Weather and Climate Extremes 29 (2020) 100262

Contents lists available at ScienceDirect

Weather and Climate Extremes

journal homepage: http://www.elsevier.com/locate/wace

Factors affecting extreme rainfall events in the South Pacific

Sunil Kumar Pariyar *, Noel Keenlyside, Asgeir Sorteberg, Thomas Spengler, Bhuwan Chandra Bhatt, Fumiaki Ogawa

Geophysical Institute and Bjerknes Center for Climate Research, University of Bergen, Norway

A B S T R A C T

Extreme rainfall events in the South Pacific are widespread and affected by various factors on different time scales. We use daily rainfall data from 20 stations over the South Pacific to investigate the characteristics of extreme rainfall events from 1979 to 2018. For regional analysis, we group the stations into three clusters characterizing the western, the central, and the far eastern regions of the South Pacific Convergence Zone (SPCZ). Extreme rainfall events contribute to roughly 20% of the seasonal mean rainfall in all three clusters. Among all four factors considered, tropical cyclones (TCs) cause the highest increase in the probability ($\Delta p_{westernSPCZ}$~286%, $\Delta p_{centralSPCZ}$~84%, $\Delta p_{fareasternSPCZ}$~189%) of extreme rainfall events. The Madden-Julian Oscillation (MJO) is the second most important factor affecting the probability of extreme rainfall events, increasing it by 30–60% when the MJO is active over the western SPCZ in phases 5–6, over the central SPCZ in phases 6–7, and over the far eastern SPCZ in phases 8–1. The probability is reduced by the same order of magnitudes during the opposite dry phases of the MJO, i.e., phases 1–3 for the western and central SPCZ, and 3–6 for far the eastern SPCZ region. The probability of extreme rainfall events increases during La-Niña (El-Niño) conditions to the southwest (southeast) of the mean SPCZ by 27% (31%); however, the impact of the El-Niño and Southern Oscillation (ENSO) along the SPCZ is not apparent. Dynamical analysis shows that the favorable conditions for generating extreme rainfall events are associated with northwesterly moisture transport and its convergence. The impact of TCs, MJO, and ENSO on rainfall extreme events can be partly understood considering this dynamical analysis. Extratropical Rossby waves can trigger tropical disturbances, but their impact on extreme rainfall events is generally less important than of the TCs, MJO, and ENSO.

1. Introduction

Extreme rainfall events are often associated with severe impacts on society and the environment. The devastating impact of heavy rainfall events ranges from loss of human life and property, degradation of the environment, to the destruction of infrastructures. The small island countries in the South Pacific often experience extreme climatic events including intense rainfall events. The impacts of extreme events depend also on the societal exposure and vulnerability (Field et al., 2012). These small island countries are highly vulnerable to extreme events compared to other parts of the world, as they are smaller in size, surrounded by vast areas of ocean, and limited infrastructure facilities (McCarthy et al., 2001; Nurse et al., 2014). Considering the vulnerability and potential risk associated with extreme rainfall events, it is essential to understand the factors controlling the variability of the extreme rainfall events in the South Pacific to improve the forecast skill of extreme rainfall events so that the potential damage can be minimized.

Three tropical phenomena mainly contribute to the variability of extreme rainfall events in the South Pacific: tropical disturbances, El-Niño Southern Oscillation (ENSO), and the Madden-Julian Oscillation (MJO). Tropical disturbances, including tropical depression (TDs) and tropical cyclones (TCs) are arguably the most important source of extreme weather events in tropical regions (Dare et al., 2012; Prat and Nelson, 2013; Chen and Fu, 2015; Khouakhi et al., 2017) and the South Pacific (McCarthy et al., 2001; Salinger and Lefale, 2005; Terry, 2007; Diamond et al., 2012; Kuleshov et al., 2014; Chand et al., 2020). Every year on average there are ten tropical cyclones in the South Pacific (Diamond et al., 2012; Walsh et al., 2016). Between 1980 and 2016, at least one tropical cyclone annually has reached the intensity equivalent to a category 4 or 5 extreme cyclone in the South Pacific (Hoarau et al., 2018). The intense rainfall and winds associated with such extreme TCs often lead to widespread damage of life and property through severe floods and subsequent landslides (Zhang et al., 2009; Chen et al., 2013; Kuleshov et al., 2014; Jenkins and Jupiter, 2015). TCs, in particular, contribute up to 20% of the total seasonal rainfall in the South Pacific (Jiang and Zipser, 2010) and accounts for almost 76% of the total recorded natural disasters in the South Pacific between 1950 and 2004 (Bettencourt et al., 2006).

On seasonal to interannual time scales, ENSO causes most of the rainfall variability over the South Pacific (Philander, 1990; Kidson and Renwick, 2002; Salinger and Lefale, 2005; Zhang et al., 2014; Borlace et al., 2014; Kuleshov et al., 2014). The impact of ENSO in the South Pacific with dry and wet conditions produces favorable conditions for extreme rainfall events. In particular, the position of the South Pacific

* Corresponding author. Allegaten 70, Bergen, Norway.
E-mail address: sunil.pariyar@uib.no (S.K. Pariyar).

https://doi.org/10.1016/j.wace.2020.100262
Received 22 August 2019; Received in revised form 27 April 2020; Accepted 11 May 2020
Available online 16 May 2020

Convergence Zone (SPCZ) is primarily controlled by ENSO (Brown et al., 2011; Vincent et al., 2011) with more southwestward shift during the La-Niña phase and northeastward during the positive El-Niño phase (Trenberth, 1976; Kidwell et al., 2016). As a result, the islands to the north of SPCZ experience more extreme rainfall events during El-Niño condition and those to the south less (Salinger and Lefale, 2005). Past studies have shown that the interannual variability of frequency of extreme rainfall events in the South Pacific is linked to ENSO (McGree et al., 2014; Kuleshov et al., 2014). Likewise, the shifts in the SPCZ position in response to ENSO also affect the location and frequency of TCs (Basher and Zheng, 1995; Vincent et al., 2011; Callaghan and Power, 2011; Salinger et al., 2014), modulating the location, frequency, and intensity of extreme rainfall events.

On the intraseasonal time scale, the MJO is the dominant mode of tropical intraseasonal rainfall variability (Madden and Julian, 1994; Zhang, 2005, 2013). It influences both rainfall patterns and extremes over the South Pacific (Matthews et al., 1996; Matthews and Li, 2005; Jones et al., 2004; Chand et al., 2020). The MJO also modulates TC activity and thereby affecting the distribution of extreme rainfall events in the South Pacific (Camargo et al., 2009; Klotzbach, 2014; Chand et al., 2020).

Apart from tropical phenomena, disturbances related to extratropical Rossby waves also impact rainfall in the South Pacific (Trenberth, 1976; Vincent, 1994; Matthews et al., 1996; Kiladis and Weickmann, 1997; Widlansky et al., 2011; Allen et al., 2009; Matthews, 2012; Niznik et al., 2015). In particular, transient Rossby waves propagate from the southeastern Australian region toward the central Pacific where they can affect convective activity (Matthews, 2012; Van Der Wiel et al., 2016a; 2016b). Even though the impact of these waves on rainfall variability over the SPCZ is well known, their role in determining extreme rainfall events is not well understood (Matthews, 2012; Van Der Wiel et al., 2015).

Studies on extreme rainfall events in the South Pacific have mostly focused on interannual variability and long-term trend analysis (Manton et al., 2001; Griffiths et al., 2003; Jovanovic et al., 2012; McGree et al. 2014, 2019; Kumar et al., 2014). Although the impacts of ENSO, MJO and TC on rainfall variability over the South Pacific are known (Trenberth, 1976; Salinger et al., 2001; Folland et al., 2002; Griffiths et al., 2003; Brown et al., 2011; Vincent et al., 2011; Kidwell et al., 2016; Pariyar et al., 2019), the impact of these and other phenomena on extreme rainfall events in this region is not thoroughly understood. Therefore, we investigate the various factors affecting extreme rainfall events in the South Pacific by using the daily rain gauge and gridded reanalysis data sets for the period 1979 to 2018. We focus our analysis on quantifying the impacts of TCs, the MJO, ENSO, and extratropical Rossby waves on extreme rainfall events and identify the relevant mechanisms.

2. Data, indices, and methods

2.1. Data and indices

Our primary source of data is the daily rainfall from 33 stations over the South Pacific, obtained from the National Climate Data Center (NCDC) website (https://www7.ncdc.noaa.gov/CDO/cdoselect.cmd?datasetabbv=GSOD). The NCDC daily data undergoes extensive automated quality control to remove unrealistic and erroneous data. The quality control includes a temporal and spatial consistency check, a percentile-based climatological outlier check, and an identification of unrealistic breaks (Durre et al., 2010). In this study, we only use the daily rainfall data that were derived from either four 6-hourly or two 12-hourly values. We discard daily values that are accumulated over multiple days. Further, we also exclude stations that have a large amount of missing data, by selecting only stations in which at least 37 years between 1977 and 2018 (i.e., out of 41 years) have at least 75% of daily data during southern hemisphere extended summer season (November to April). Note that November to April is the rainy season in the South Pacific (Fig. 2). Based on these criteria, we chose only 20 stations out of 33 for further analysis. The 20 selected rainfall stations are distributed over the South Pacific region, representing many island countries and extending along the SPCZ from the southwest to the far east (Fig. 1; Supplementary Table S1). Even though the NCDC data has gone through the standard quality control procedure, we further perform a homogeneity test by using the RHtest software package (Wang and Feng, 2013) developed at Climate Research Division, Atmospheric Science and Technology Directorate, Science and Technology Branch, Environment Canada (http://etccdi.pacificclimate.org/software.shtml). In particular, we use RHtests_dlyPrcp package for homogenization of daily precipitation data (Wang et al., 2010). In this software package, any discontinuity in the rainfall time series is identified through the penalized maximal *t*-test (Wang et al., 2007) and the penalized maximal F-test (Wang, 2008a); in which the multiple-phase linear regression algorithm is embedded (Wang, 2008b). This method is suggested to be effective in detecting the change points in daily rainfall data that are consistent with the documented discontinuities (Wang et al., 2010). The statistically significant (95% confidence level) change points are then adjusted based on Quantile-Matching (QM) adjustment method (Wang et al., 2010; Vincent et al., 2012). Note that for stations with the metadata information, the identified change points are verified with the metadata and then adjusted; whereas for stations without metadata information, only statistically significant change points are adjusted. We then use the adjusted homogeneous data for 20 stations for further analysis.

We use three additional data sets that cover the period 1979 to 2018 to investigate the synoptic conditions associated with extreme rainfall events. First, we use 6-hourly ERA-Interim data set at 0.75° horizontal resolution (Dee et al., 2011) to identify the atmospheric conditions associated with extreme rainfall events. Second, we use daily interpolated outgoing long-wave radiation (OLR) data with a horizontal resolution of 2.5° provided by the National Oceanic and Atmospheric Administration (NOAA) (Liebmann and Smith, 1996). We use this data to represent the large-scale spatial structures of the convection associated with extreme rainfall events. Third, we use the satellite-derived monthly Global Precipitation Climatology Project (GPCP) gridded precipitation data set to compute the long-term rainfall climatology as shown in Fig. 1 (Adler et al., 2003). We use the GPCP combined precipitation data version 2.3 with a horizontal resolution of 2.5°.

We use two climate indices: the real-time multivariate MJO (RMM) indices and the monthly Niño3.4 ENSO index. The daily RMM indices are from the Australian Bureau of Meteorology website (http://www.bom.gov.au/climate/mjo/). The two RMM indices (RMM1 and RMM2)

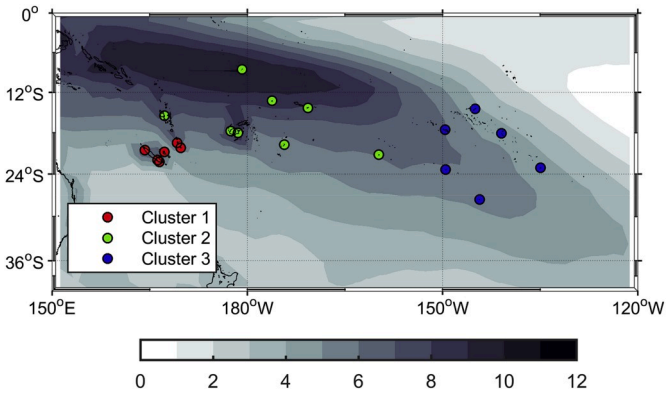

Fig. 1. Location of rain gauge stations used in this study. The three clusters of stations are indicated by red, green, and blue colours. The shaded contours are the rainfall climatology (1979–2018) in mm day^{1}, computed from the monthly GPCP gridded data set. (For interpretation of the references to colour in this figure legend, the reader is referred to the Web version of this article.)

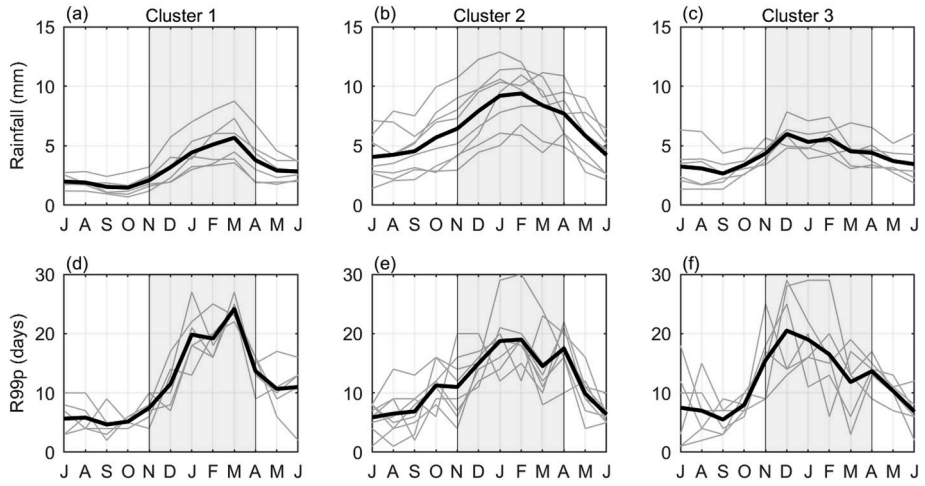

Fig. 2. (a–c) Rainfall annual cycle based on monthly total rainfall (mm day^{-1}) for six, eight, and six stations in cluster 1, cluster 2, and cluster 3, respectively. (d–f) Annual cycle of extreme rainfall events based on the monthly frequency of extreme rainfall events. Extremes rainfall events are defined as daily rainfall values greater than the 99th percentile. The grey lines are for individual stations, and the black lines are the mean of all stations.

are the first two leading principal components obtained from the combined empirical orthogonal function analysis of daily OLR, 850 hPa zonal wind and 200 hPa zonal wind averaged over 15°S-15°N (Wheeler and Hendon, 2004). We define the active MJO events as those in which the normalized principal component amplitudes are higher than one (i.e., $RMM1^2+RMM^2>1$). The RMM indices are largely dominated by large-scale circulation and may not necessarily represent the local or regional convection (Zhao et al., 2013). Therefore, for comparison we also use the all-season outgoing longwave radiation-based MJO index (OMI) (Kiladis et al., 2014). The OMI is based on the empirical orthogonal function analysis of daily OLR time series and thus expected to better represents local to regional convection compared to the RMM indices. However, the conditional probability analysis based on OMI and RMM indices is fairly comparable, therefore we only present the analysis based on RMM indices in this study. We compute the monthly Niño3.4 index from the monthly sea surface temperature (SST) from the NOAA, ESRL, Physical Science Division website (http://www.esrl.noaa.gov/psd/gcos_wgsp/Timeseries/Niño34/index.html). The Niño3.4 index is defined as the SST anomalies averaged from 5°S-5°N and 170°W-120°W (Rayner et al., 2003). To define the different phases of ENSO, namely El-Niño, La-Niña, and neutral, we compute the five-month running mean of the Niño3.4 index. We define El-Niño (La-Niña) years when the five-month running mean Niño3.4 index is higher (lower) than 0.4 °C (−0.4 °C) for six or more consecutive months, and we define other years as neutral years (Trenberth, 1997).

TC data is from the International Best Track Archive for Climate Stewardship (IBTrACS) (Knapp et al., 2010). The IBTrACS data set is based on the 6-hourly historical TC records from various sources and it provides information on the nature of the storm, location of the storm center, maximum sustained winds, minimum central pressure, and storm speed. We consider an extreme rainfall event to be induced by a TC if there was a TC within a 500 km radius of the station. We define such an event as a tropical cyclone day (TCD). The choice of the 500 km radius is common in TC analysis (Rodgers et al., 2001; Larson et al., 2005; Jiang and Zipser, 2010; Lee et al., 2010; Dare et al., 2012; Prat and Nelson, 2013; Villarini et al., 2014). To understand the sensitivity to the radius size, we repeated the analysis for different radii between 500 and 700 km and observed no significant difference in our results.

2.2. Station clustering and definition of extreme rainfall events

To better understand the spatial distribution of extreme rainfall events, we group the 20 stations into three clusters according to the following criteria: members (stations) of a cluster must have a similar daily rainfall climatology (Fig. 1), and have similar seasonal cycles of both monthly mean rainfall (Fig. 2a–c) and frequency of extreme rainfall events (Fig. 2d–f). The three clusters represent the rainfall variability and extremes over the western SPCZ (cluster 1, with six stations), the central SPCZ (cluster 2, with eight stations), and the far eastern SPCZ (cluster 3, with six stations) (Fig. 1). The climatology of mean monthly rainfall and frequency of extreme rainfall events peaks in March, January–February, and December for most of the station in cluster 1, cluster 2, and cluster 3, respectively (Fig. 2a–f).

We tested the k-means clustering algorithm as a more objective means to define the clusters (Robertson and Ghil, 1999), but the results were not satisfactory. The algorithm groups stations into a pre-defined number of clusters such that the sum of the squared Euclidean distance is minimized. We used daily rainfall data to estimate the correlation coefficients between different stations, and based on these correlation coefficients, we compute the Euclidian distances within the set of clusters. We estimated the optimal number of clusters using three different methods: the elbow method (Ketchen and Shook, 1996; Ghayekhloo et al., 2015), the average silhouette method (Rousseeuw, 1987; Kaufman and Rousseeuw, 2009), and the gap statistics method (Tibshirani et al., 2001). However, the optimal cluster size differed among the three methods. Thus, we did not use the k-means method to define the clusters.

We categorize the daily rainfall exceeding the 99th percentile as extreme rainfall events. The 99th percentile is computed for each station for data from November to April between 1979 and 2018. The total number of events in a cluster is the sum of all the events at all available stations within the cluster. Note, events that occurred on the same day at multiple stations within a cluster are considered as the same event and counted only once.

2.3. Statistical methods

We express the frequency of extreme rainfall events in terms of probability instead of absolute frequency. The probability of extreme rainfall events occurring in a cluster is defined as the total number of extreme rainfall events at all stations in the cluster divided by the total number of calendar days considered. The baseline probability of extreme rainfall events in each cluster is computed using all available days (i.e., unconditional probability). The baseline probabilities in cluster 1, cluster 2, and cluster 3 are 4.3%, 6.9%, and 5.3%, respectively; note given our definition these numbers partly reflect the number of stations. We quantify the impact of various phenomena on extreme rainfall events by computing conditional probabilities. The conditional

probability of event A given event B is defined as the ratio of the probability of A and B occurring together (unconditional) to the probability of event B. For example, the conditional probability of an extreme rainfall event occurring during the MJO phase 5 is the probability of extreme rainfall and MJO phase 5 occurring together divided by the probability of MJO phase 5 occurring. We use this approach to compute the conditional probability of extreme rainfall events for all eight phases of the MJO, all three phases of ENSO, for TCDs, and for extratropical Rossby wave activity. We use the bootstrap resampling approach to test statistical significance of the probability estimates (Muñoz et al., 2015).

We study the synoptic conditions associated with extreme rainfall events by generating composites of selected atmospheric variables including sea level pressure (SLP), vertically integrated moisture flux divergence (qdiv), 850 hPa wind (both u and v components), evaporation, outgoing long-wave radiation (OLR), and 300 hPa geopotential height. The daily total evaporation is computed by summing the cumulative evaporation of two 12-hourly forecasts. We compute the horizontal wave activity flux following the method of Takaya and Nakamura (2001) and using daily 300 hPa wind (u,v) and geopotential height data. To quantify the impact of extratropical waves on extreme rainfall events, we define a wave index following Wallace and Gutzler (1981) and based on this we compute the conditional probability of extreme rainfall events during positive and negative wave events as before. We compute the statistical significance of the composite analysis using the bootstrap resampling approach (Muñoz et al., 2015).

3. General characteristics of daily rainfall and extremes

In this section we discuss the key characteristics of extreme rainfall events in three clusters over the South Pacific. We first compare the statistics of daily rainfall and extreme rainfall events among the three clusters, so as to understand the spatial distribution of extreme rainfall events over the South Pacific. We then discuss the interannual variability of the extreme rainfall events in the three clusters. This includes extreme contribution to seasonal rainfall and the relationship between extreme rainfall events and ENSO on interannual time scale.

3.1. Distribution of daily rainfall and extreme rainfall events

We compute the statistics characterizing the daily rainfall and rainfall extremes in each cluster considering all available daily rainfall data from 1979 to 2018 for all stations in each cluster (Table .1). We define extreme rainfall events for each individual station before we combine all the events from all stations in each cluster. The total number of extreme rainfall events in cluster 1, cluster 2, and cluster 3 are 331, 532, and 410, respectively. The difference among clusters is mainly because the amount of data in each cluster is different, as there are six stations in cluster 1 and cluster 3, and eight stations in cluster 2, and the number of missing data at each station is different.

The mean (μ), and standard deviation (SD) of the daily rainfall data are highest in cluster 2 (Table 1), compared to the remaining two clusters. This is consistent with cluster 2 coinciding with the region of higher mean and variability of rainfall in the SPCZ (Vincent et al., 2011; He et al., 2017). Interestingly, the percentile values (95th and 99th percentile) are also highest in cluster 2. Among the three clusters, the daily rainfall statistics have the lowest values in cluster 1. The mean intensity of rainfall extremes (μ~139.7 mm day^{-1}) is highest in cluster 2, while the other two clusters have quite comparable values. Despite cluster 2 having by far the highest mean extreme rainfall intensity, the standard deviation of extreme rainfall and the percentile values in cluster 1 and cluster 2 are quite comparable. This implies that extreme rainfall events in cluster 1 can be as intense as those in cluster 2. On the other hand, cluster 3 has substantial lower standard deviations and the percentile values than the other two clusters.

Table 1
Summary statistics of daily rainfall and rainfall extremes in November–April from 1979 to 2018.

Daily rainfall				
	Mean (mm)	SD (mm)	95th percentile (mm)	99th percentile (mm)
Cluster 1	3.6	13.9	19.8	62.9
Cluster 2	7.6	19.0	39.9	89.3
Cluster 3	4.7	14.0	26.9	68.1
Daily extreme rainfall events				
Cluster 1	105.8	62.3	229.8	350.5
Cluster 2	139.7	57.9	265.7	379.5
Cluster 3	100.6	42.3	169.5	269.5

3.2. Interannual variability of daily rainfall extremes

We now discuss the interannual variability of extreme rainfall events in terms of probability and intensity. For each extended southern hemisphere summer season (November–April), we compute the probability and mean intensity of extreme rainfall events. On average, the probabilities of extreme rainfall events per season are 4.3%, 6.9% and 5.3% in cluster 1, cluster 2, and cluster 3, respectively. However, there is a large year-to-year variability in the probabilities of extreme rainfall events, as indicated by the large range in probabilities: 0–10.9%, 2.1–12.6%, and 0.5–14.3% for cluster 1, cluster 2, and cluster 3, respectively.

We assess the relationship between ENSO and the interannual variability of extreme rainfall events by computing the Spearman's rank correlation coefficient. There is a statistically significant relation (at the 95% level) between the seasonal mean Niño3.4 index and the seasonal frequency of extreme rainfall events in each of the three clusters. The correlation coefficients are −0.23, 0.29, and 0.45 for cluster 1, cluster 2, and cluster 3, respectively. We observe a similar relationship between the Niño3.4 index and seasonal mean extreme rainfall with higher (lower) rainfall amount during El-Niño (La-Niña) in cluster 2 and cluster 3. The opposite is true for cluster 1. The respective correlation coefficients are −0.33, 0.29, and 0.44 in cluster 1, cluster 2, and cluster 3. All three correlation coefficients are significant at 95% level. The analysis of ENSO impacts on extreme rainfall is investigated further in section 4.

We compute the contribution of extreme rainfall events to the total seasonal rainfall by summing up the rainfall amounts associated with extreme rainfall events in each season (November–April) and dividing by the total seasonal rainfall. On average, extreme rainfall contributes 24.5%, 15.8%, and 18.8% to the total rainfall in cluster 1, cluster 2, and cluster 3, respectively. Extreme rainfall contributions to seasonal totals shows large interannual variability in all three clusters (Supplementary Fig. S1) with values ranging from 8.4 to 47.7%, 2.3–27.2%, and 5.0–34.2% in cluster1, cluster 2, and cluster 3, respectively. Interestingly, the interannual variability of extreme rainfall contributions is fairly comparable to the variability of total seasonal rainfall. The correlation coefficients between the extreme rainfall contributions to seasonal totals and total seasonal rainfall are 0.88, 0.67, and 0.83 for cluster 1, cluster 2, and cluster 3, respectively. All three correlation coefficients are statistically significant at the 99% confidence level.

3.3. Influence of TCs, MJO, and ENSO on extreme rainfall events

We now assess the influence of TCs, ENSO, and the MJO on extreme rainfall events in terms of whether the probability of an extreme rainfall event is affected by TCD, or different phases of the MJO and ENSO (section 2.3). In particular, we present the percentage change in probability, Δp, computed by subtracting the baseline probability from the conditional probability and dividing by the baseline probability and then multiplying by 100.

The total number of TCDs observed over the study period is considerably higher in cluster 2 (TCDs~664), compared to cluster 1

(TCDs~352), and cluster 3 (TCDs~144). This is consistent with the typical spatial distribution of TC density in the South Pacific, with higher TC densities along the SPCZ and relatively lower densities to the southwest and northeast of the mean SPCZ region (Dowdy et al., 2012). However, the higher number of TCDs in cluster 2 could also be because of the higher number of stations in this cluster compared to the other two clusters. To assess whether this is the case, we compute the average number of TCDs per station in each cluster (i.e., the number of TCDs divided by the total number of stations). The average TCDs per station are 58.7, 83.0, and 24.0 in cluster 1, cluster 2, and cluster 3, respectively. This shows that cluster 2 does indeed have the greatest frequency of TCDs and that cluster 3 has the least. Out of all TCDs, only 55, 57, and 16 TCDs are associated with extreme rainfall events in cluster 1, cluster 2, and cluster 3, respectively. This indicates that only 16.6%, 10.8%, and 4.0% of the total number of extreme rainfall events are associated with TCs in cluster 1, cluster 2, and cluster 3, respectively.

Of the factors we analysed, TCs are the most important one affecting extreme rainfall events in the South Pacific. The probability of extreme rainfall events is substantially increased when there is a TCD (Fig. 3a). In particular, it is increased by 285.5%, 84.2%, and 188.6% in cluster 1, cluster 2, and cluster 3, respectively. All three values are statistically significant at the 99% level. Most of the TCs that induced extreme rainfall events in our region originated from the region between 0°-20°S (as indicated by green dots in the Supplementary Fig. S2) and moved to the higher latitudes in a southeastward direction. This is consistent with the usual trajectories for TCs in the South Pacific (e.g., Diamond et al., 2012; Dowdy et al., 2012; Khouakhi et al., 2017).

It is well known that TCs are often associated with intense rainfall events over the tropical region (Nogueira and Keim, 2011; Dare et al., 2012; Ng et al., 2015); therefore, it is interesting to investigate whether the intensities of extreme rainfall events are also high during TCDs. The distribution of daily rainfall magnitudes for all extreme rainfall events with and without TCs are presented in the form of box plots (Fig. 3b). Note that the upper whiskers in the box plots are the 99th percentile. For cluster 1, the 75th percentile is considerably higher for daily extremes associated with TCs than for extremes that were not associated with TCs, but the 99th percentiles are comparable for the extremes that occurred with and without TCs. For the rest of the clusters, both the 75th and 99th percentiles are lower for the extreme rainfall events that occurred with TCs than occurred without. This suggests that TCs do not necessarily contribute to the most extreme rainfall events, especially in cluster 2 and cluster 3.

We now assess the impact of the MJO on extreme rainfall events. The probability of extreme rainfall events is generally increased in cluster 1, cluster 2, and cluster 3 during MJO phases 5–7, 6–8, and 7–1, and decreased in phases 1–3 in cluster 1 and cluster 2, and phases 2–6 in cluster 3 (Fig. 4a–c). The maximum positive departure in probability is observed in phase 5 (Δp ~ 51.6%), phase 7 (Δp ~ 51.5%), and phase 8 (Δp ~ 64.2%) in cluster 1, cluster 2, and cluster 3, respectively. While the maximum reduction in probability is observed during phase 2 in cluster 1 (Δp ~ −42.4%) and cluster 2 (Δp ~ −28.3%), and phase 4 in cluster 3 (Δp ~ −29.4%).

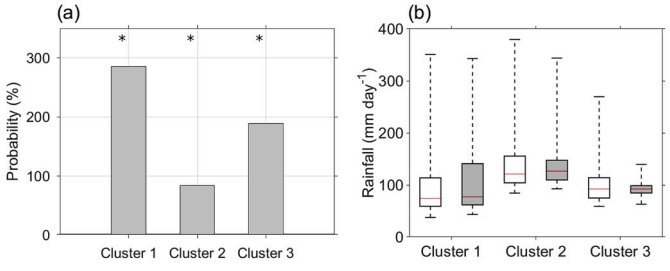

Fig. 3. (a) Percentage change in the probability of extreme rainfall events for TCDs with respect to the baseline probability for all extreme events. The significant values at the 99% (95%) confidence level are denoted by a single (double) star, computed using a bootstrap resampling method by randomizing the time series 1 000 times. (b) Box plots of daily rainfall extremes (mm day^{-1}) without (white box) and with TC (grey box) in each cluster. Lower and upper whiskers denote the minimum and 99th percentiles. The lower, middle, and upper lines in the box represent the inter-quartile range.

These changes in probabilities are related to active or suppressed convection during the particular MJO phase. Similarly, the MJO's eastward progression causes its impact on the probability of extreme rainfall events to shift to later phases from cluster 1 to cluster 3. These effects are illustrated by showing the OLR and 850 hPa wind anomalies for all eight phases of the MJO together with the location of the clusters (Fig. 4d–k). The MJO phase 5 composite shows pronounced negative OLR anomalies and northwesterly wind over cluster 1 (Fig. 4h). While in phases 6–7, the OLR and wind anomalies are shifted to the east and located about cluster 2 (Fig. 4i and j). In phases 1, 7, and 8, the enhanced convection is furthest east and is located about cluster 3 (Fig. 4k,d). During the opposite dry phases, the rainfall is suppressed and easterly to southeasterly wind dominates the South Pacific region. For example, during phases 1–3, positive OLR anomalies dominate region corresponding to cluster 1 and cluster 2 (Fig. 4d–g). Similarly, during phases 3–5, the convection is suppressed over the region covering cluster 3 (Fig. 4e–h).

As discussed in section 3.2, the interannual variability of extreme rainfall events in the South Pacific is somewhat modulated by ENSO (McGree et al., 2014). Our analysis shows that the probability of extreme rainfall events varies in different phases of ENSO (Fig. 5a–c). In particular, the probability of extreme rainfall events increases by 27.3% during La-Niña conditions in cluster 1, by 31.2% during El-Niño conditions in cluster 3, and, by a rather small 5.1% during the neutral conditions in cluster 2. Note that the increase in probability in cluster 1 and cluster 3 are statistically significant at the 99% confidence level, but for cluster 2, it is only significant at the 95% level. Likewise, the reduction in extreme rainfall events during La-Niña phase in cluster 3 (Δp ~ −17.8%) and cluster 2 (Δp ~ −16.4%) are also significant at the 95% confidence level.

Evidence for the large-scale impact of ENSO in the South Pacific is shown in terms of composites of OLR and 850 hPa wind for El-Niño and La-Niña conditions (Fig. 5d and e). During El-Niño events, the large-scale wind patterns show westerly wind anomalies with wet conditions over the equatorial and southeastern Pacific. Meanwhile, to the southwest of the mean SPCZ, dry conditions dominate with positive OLR anomalies (Fig. 5d). These changes reflect an equatorward and more zonal orientation of the SPCZ during El-Niño; opposite conditions are found during La-Niña (Fig. 5e) (Trenberth, 1976; Folland et al., 2002; Brown et al., 2011; Vincent et al., 2011).

These changes associated with rainfall can only partly explain the ENSO impacts on rainfall extremes in the region. In particular, La-Niña causes the region to the southwest of the SPCZ to be wetter and the region to the east to be drier (Fig. 5e), and this is consistent with the impacts on extreme rainfall events in clusters 1 and 3. On the other hand, El-Niño has its most pronounced impact on extremes in cluster 3, but the atmospheric conditions in this region show little or no change; while the atmospheric conditions in cluster 1 and cluster 2 are clearly dry, but the impacts on extremes in these clusters is minimal. The difficulties in explaining ENSO impacts on extreme rainfall events could be partly because the clusters extend over quite large domains.

4. Physical basis of extreme rainfall events

To better understand the physical mechanism, we analyze the synoptic conditions associated with extreme rainfall events in each cluster. For this, we prepare the anomaly composites of selected atmospheric fields for all extreme rainfall events. The variables used are OLR, SLP, 850 hPa wind, vertically integrated specific humidity (from the surface up to 200 hPa), vertically integrated moisture flux divergence, evaporation, and 300 hPa geopotential height. First, we present the general

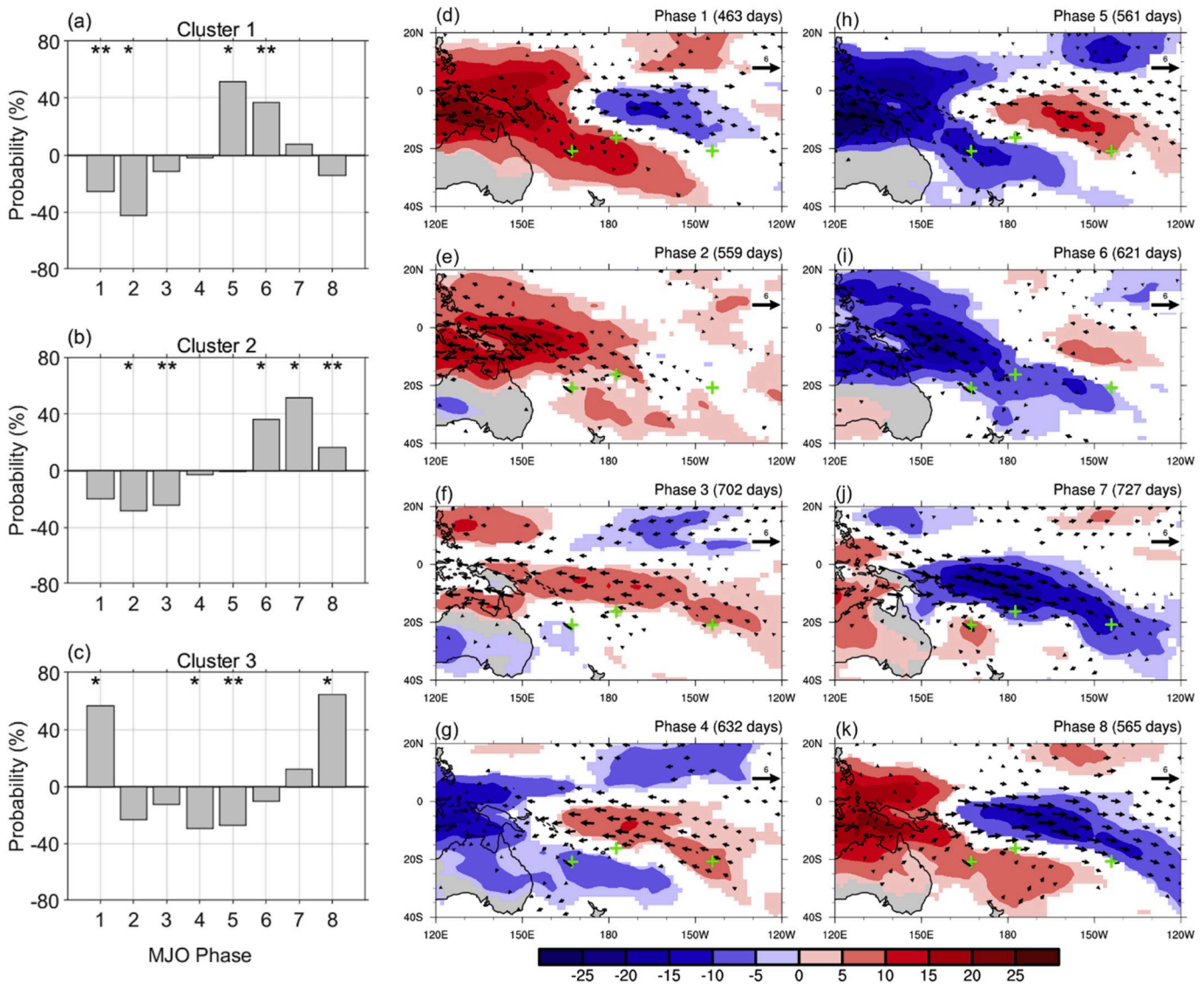

Fig. 4. (a–c) Percentage change in the probability of extreme rainfall events for each of eight phases of the MJO with respect to the baseline probability. A single (double) star denotes the significant values at the 99% (95%) confidence level. (d–k) Anomaly phase composites of OLR (shaded, w m^{-2}) and 850 hPa wind (vector, m s^{-1}) for all eight phases of the MJO. Only significant values at the 95% confidence level are shown, computed using a bootstrap resampling method by randomizing the time series 1 000 times. The approximate central location of each cluster is represented by a green marker with a plus sign.

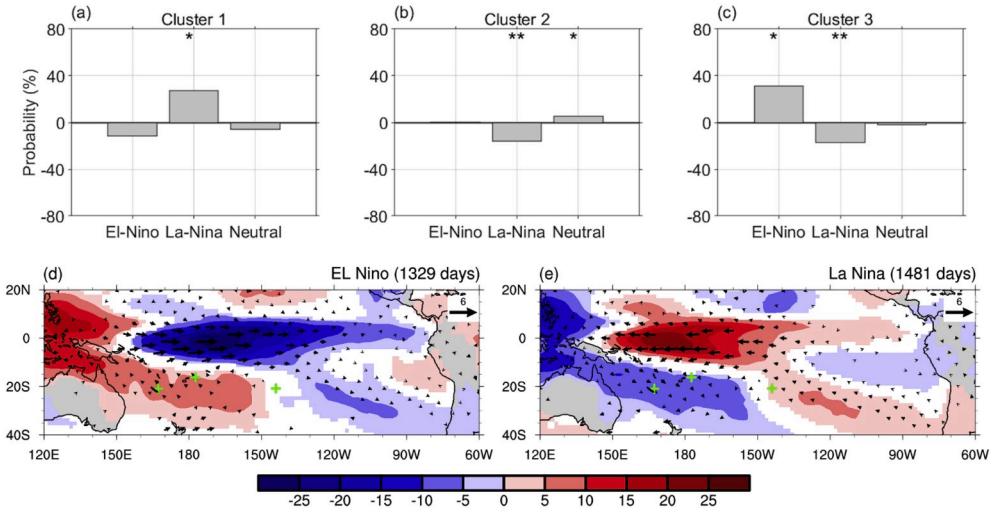

Fig. 5. (a–c) Percentage change in the probability of extreme rainfall events for El-Niño, and La-Niña phase of ENSO with respect to the baseline probability. A single (double) star denotes the significant values at the 99% (95%) confidence level. (d–e) Anomaly phase composites of OLR (shaded, w m^{-2}) and 850 hPa wind (vector, m s^{-1}) for El-Niño and La-Niña conditions. Only significant values at the 95% confidence level are shown, computed using a bootstrap resampling method by randomizing the time series 1 000 times. The approximate central location of each cluster is represented by a green marker with a plus sign.

atmospheric conditions associated with all extreme rainfall events. Second, we show lag-composites of 300 hPa geopotential height to illustrate the influence of extratropical Rossby waves on extreme rainfall events. Third, we briefly discuss the mechanisms of how different phases of the MJO and ENSO help to produce extreme rainfall events in each cluster.

4.1. General atmospheric conditions

During extreme rainfall events in all three clusters, a low-pressure SLP anomaly is observed (Fig. 6a–c). To the northeast of the low-pressure center, strong northwesterly wind anomalies are present that are collocated with the maximum convection, which is indicated by strong negative OLR anomalies. As expected, the atmosphere is anomalously moist in the region of enhanced convection; this is indicated by positive specific humidity anomalies (Fig. 6g–i). The buildup of moisture in these regions is associated with moisture convergence, which is likely the result of the transport of moisture by the northwesterly wind anomalies (Fig. 6d–f). The surface evaporation tends to show negative anomalies in the region of convection and strong positive anomalies along the south western flank of the low-pressure center. Because the surface evaporation tends to be negative in the region with active convective, local changes in evaporation may not directly contribute to extreme rainfall events.

The time evolution of the atmospheric fields shows that the low-pressure system has already developed two to three days prior to the composite extreme rainfall events (not shown). It is the development of the low-pressure system that produces the anomalous cyclonic circulation and intensifies the northwesterly flow. Interestingly, the vertically integrated moisture flux convergence maximizes one day prior to composite extreme rainfall events. The longitude-height profile of vertical velocity (not shown) also shows a pronounced upward motion one day prior to composite extreme rainfall events, but the vertical velocity anomalies are strongest during the day of the event. The day after composite extreme rainfall events, the low-pressure anomalies weaken, the cyclonic circulation becomes less noticeable, and the northwesterly

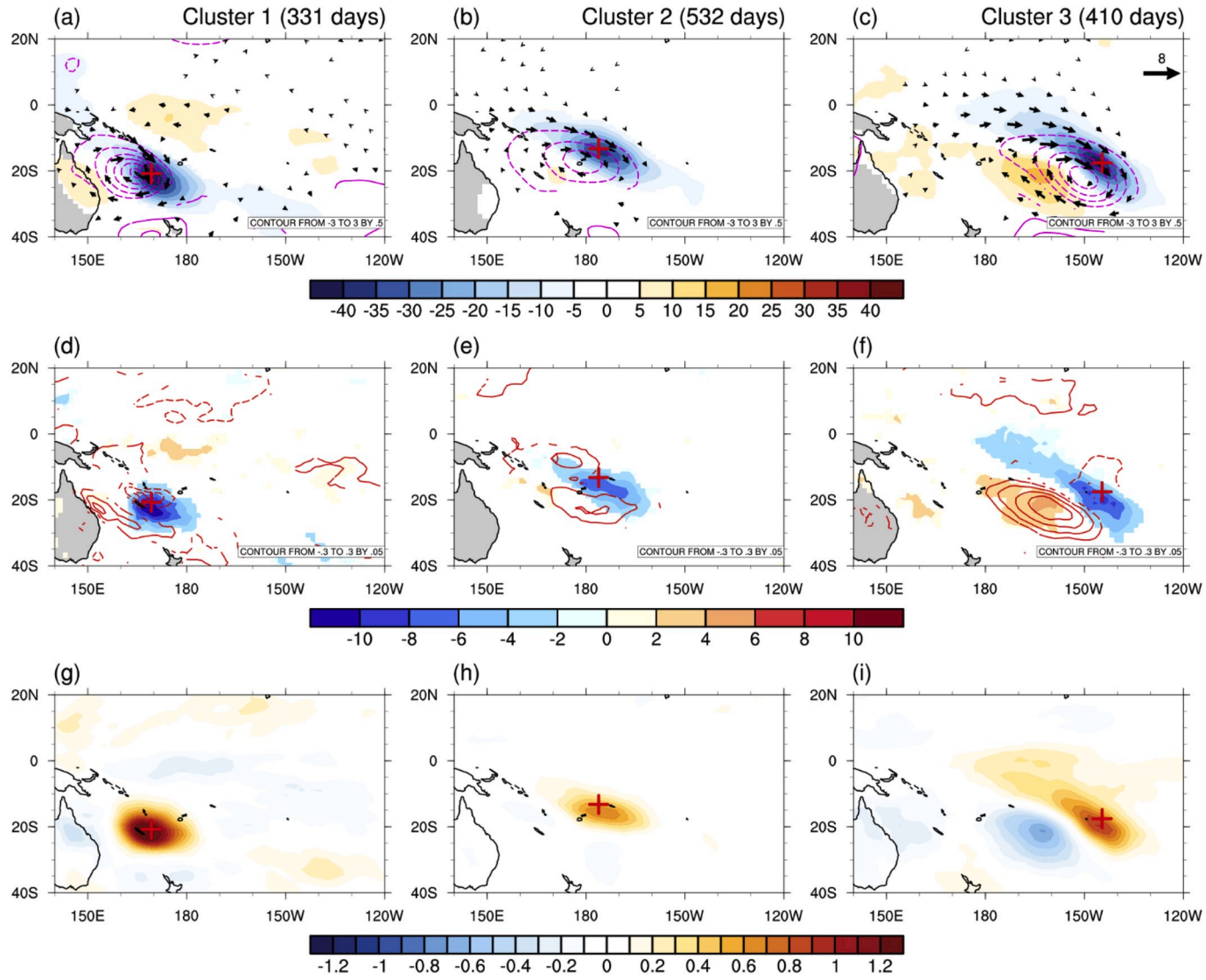

Fig. 6. Anomaly phase composites of (a–c) OLR (shaded, w m^{-2}), SLP (contours, hPa), and 850 hPa wind (vectors, m s^{-1}) for all extreme rainfall events in each cluster, (d–f) Vertically integrated moisture flux divergence (shaded, 10^{-5} kg m^{-2} s^{-1}) and evaporation (contours, mm day^{-1}) for each cluster, (g–i) vertically integrated specific humidity (kg kg^{-1}). Only significant values at the 95% confidence level are shown, computed using a bootstrap resampling method by randomizing the time series 1 000 times. The approximate central location relative to the stations in each cluster is represented by a red marker with a plus sign. The dashed (solid) contours represent negative (positive) values. (For interpretation of the references to colour in this figure legend, the reader is referred to the Web version of this article.)

wind anomalies are reduced significantly.

The low-pressure system associated with the composite extreme rainfall events in each cluster looks like a tropical depression. However, a quantitative analysis shows that these low-pressure anomalies are not related to the tropical depressions, i.e., out of all extreme rainfall events only 20, 19, and 6 events are associated with the tropical depression in cluster 1, cluster 2, and cluster 3, respectively. Therefore, the low-pressure system associated with extreme rainfall events are mostly related to other tropical disturbances, which are more likely associated with equatorward propagation of extratropical waves, as discussed next.

4.2. Role of extratropical disturbances

Composites based on extreme rainfall events show Rossby wave-like patterns between 30°S and 60°S for all three clusters (Fig. 7). We observe the development of strong wave-like patterns two days before composite extreme rainfall events. These wave trains are already established five to six days before composite extreme rainfall events (not shown). To better understand the potential impact of these waves on extreme rainfall events, we define a wave index following Wallace and Gutzler (1981). In their study, they defined the Pacific North American wave index by combining the normalized geopotential height anomalies at four different locations corresponding to the geopotential height anomaly patterns. In our case, we define wave indices by considering only three points, corresponding to the largest anomalies in the geopotential height associated with composite extreme rainfall events, as indicated by the green plus signs in Fig. 7. The daily wave indices are computed by averaging the two standardized geopotential height anomalies for locations in the pattern with the same sign and subtracting

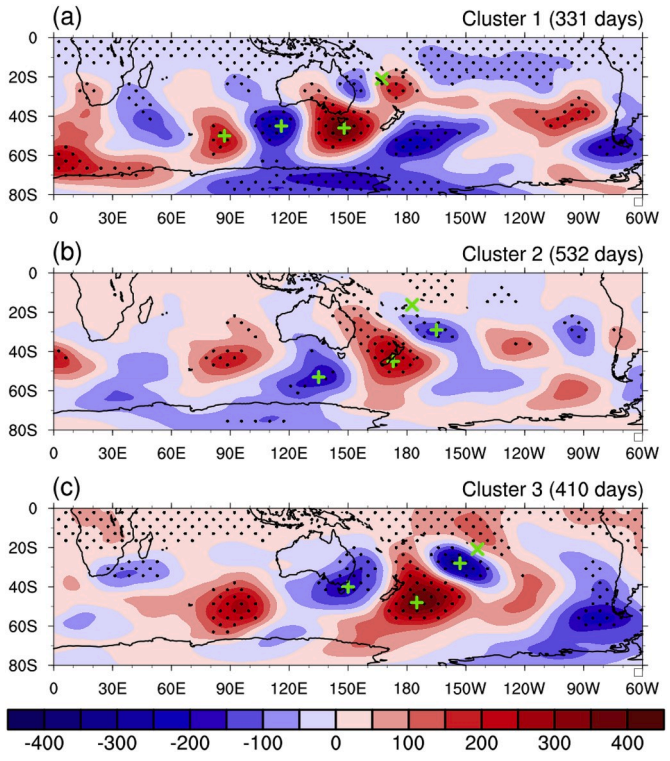

Fig. 7. Anomaly composites of 300 hPa geopotential height anomalies (m) two days prior to extreme rainfall events. A green plus sign denotes the grid point selected for the wave index calculation. The black dots denote statistically significant values at the 90% confidence level, computed using a bootstrap resampling method by randomizing the time series 1 000 times. The approximate central location relative to the stations in each cluster is represented by a green marker with a cross sign. (For interpretation of the references to colour in this figure legend, the reader is referred to the Web version of this article.)

the other standardized geopotential height anomaly from the location in pattern with the opposite sign. The sign of the indices are chosen such that positive values correspond to the patterns shown in Fig. 8. We further normalize the daily wave indices by their respective time standard deviations. From the daily normalized wave indices, we compute the probability of extreme rainfall events for the positive and negative phases of wave events similar to that of the MJO, ENSO, and TCs. We define positive (negative) wave events when the normalized wave index is higher (lower) than 1 (−1) standard deviation. Note that the positive events are defined such a way that the positive wave events correspond to low pressure anomaly at the cluster location and vice versa.

To further confirm the impact of Rossby waves on extreme rainfall events in the South Pacific, we compute the wave activity flux based on the daily anomalies of 300 hPa geopotential height and wind (u and v components). The wave activity flux that occurs from two days prior to extreme rainfall events until two days after is computed by composite analysis, considering only positive wave events (Fig. 8). Wave activity vectors indicate the paths travelled by Rossby waves; the source of waves is indicated by divergence of the vectors, while their impacts on weather patterns often occurs where the vectors convergence (Takaya and Nakamura, 1997). In general, there is a close agreement between the propagation of the Rossby wave patterns and the wave activity vectors. In addition to the strong zonal component of wave propagation, the wave activity vectors exhibit northeastward component that suggests the propagation of wave energy from higher latitudes towards the low-pressure center at each cluster. For example, for cluster 1, the wave energy propagates from the southeastern part of Australia two days prior to composite extreme rainfall events (Fig. 8a, top panel). Similarly, for cluster 2 and cluster 3, strong wave propagations are observed between the dateline and 150°W two days prior to composite extreme rainfall events (Fig. 8b and c, top panel).

The connection of extreme rainfall events and extratropical waves is further confirmed by computing the probabilities of positive Rossby wave index values during extreme rainfall events. Out of 331, 532, and 410 extreme events 89, 125, and 121 events are associated with positive wave events in cluster 1, cluster 2, and cluster 3, respectively, i.e., roughly 26.8%, 23.5%, and 29.5% of extreme rainfall events in cluster 1, cluster 2, and cluster 3 are associated with extratropical disturbances. Note that the positive phase for wave activity corresponds to the geopotential height anomaly pattern presented in Fig. 8 for all three clusters. The positive Rossby wave index values greater than one standard deviation increase probability of extreme rainfall events in cluster 1 and cluster 3 by 43.3% and 59.8% (both significant at the 95% confidence level), but in the case of cluster 2, the increase in probability is 25.3% and this value is not statistically significant at 95% level. During the negative phase of wave index, the probability of extreme rainfall events is reduced in all three clusters, but the magnitudes of the changes are little lower ($\Delta p_{\text{cluster 1}} \sim -30.8\%$; $\Delta p_{\text{cluster 2}} \sim -27.3\%$; $\Delta p_{\text{cluster 3}} \sim -35.7\%$). All three changes in probabilities for the negative phase of the wave index are not statistically significant at 95% level. From this, we may conclude that the connection between extratropical disturbances and extreme rainfall events in the South Pacific is rather weak. In particular, the extratropical wave events are quite common in the South Pacific with probabilities ranging from 17 to 18% for both positive and negative wave events. However, only few extreme rainfall events in the three clusters are associated with extratropical disturbances.

4.3. Mechanisms for TCs, MJO, and ENSO

One of the key ingredients for the occurrence of extreme rainfall events is the availability of moisture and its convergence (O'Gorman and Schneider, 2009). Therefore, to understand the mechanisms on how TCs, ENSO and the MJO modulate extreme rainfall, we compute the composites for these three phenomena of vertically integrated moisture flux divergence, vertically integrated specific humidity (from the surface to 200 hPa), and 850 hPa wind. For TCs, we compute the composites for all

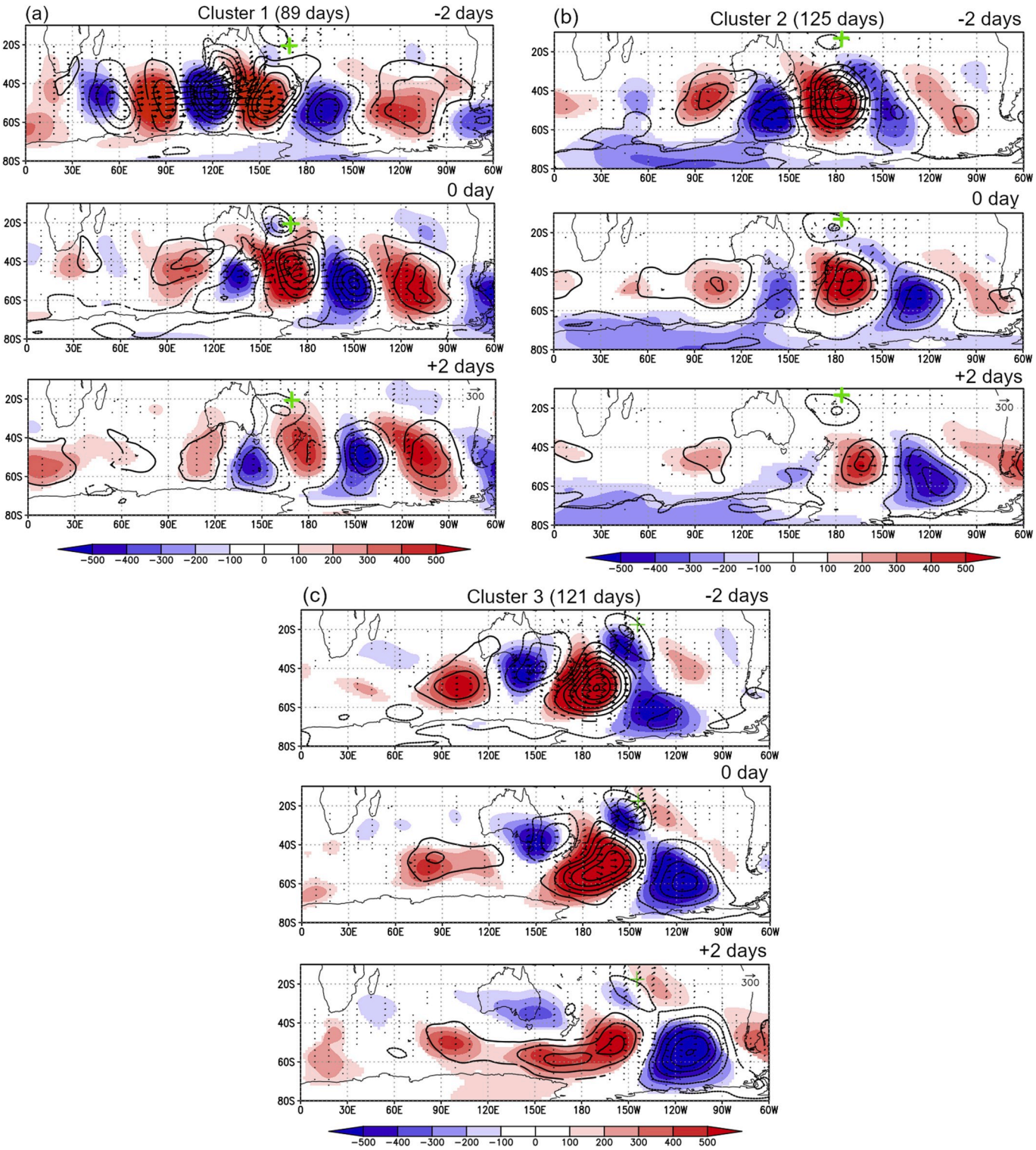

Fig. 8. Anomaly lag composites of 300 hPa geopotential height (shaded, m), wave activity flux (vectors, $m^2\ s^{-2}$), and sea level pressure (contour, hPa, contour interval 1, beginning at ±1) for (a) cluster 1, (b) cluster 2, and (c) cluster 3. The composites are shown for two days prior to the event (top panel), the day of the event (middle panel), and two days after the event (bottom panel). Only significant values at the 90% confidence level are shown, computed using a bootstrap resampling method by randomizing the time series 1 000 times. The approximate central location of each cluster is represented by a green marker with a plus sign. (For interpretation of the references to colour in this figure legend, the reader is referred to the Web version of this article.)

available TCDs in each cluster (Fig. 9a–f). Similarly, for the MJO and ENSO, we compute the composites for different phases of the MJO (Fig. 10a–f) and ENSO (Fig. 11a and b). Note that for the MJO, we show composites only for phases that correspond to the maximum change in probability of extreme rainfall events in each cluster (i.e., phase 5 for cluster 1; Phase 7 for cluster 2; Phase 8 for cluster 3). For comparison, we also show the composites for respective opposite MJO phases.

TCs seem to intensify the general atmospheric conditions for extreme rainfall events in all three clusters (Fig. 9a–c). In particular, the atmospheric patterns described in Fig. 6 are generally enhanced with

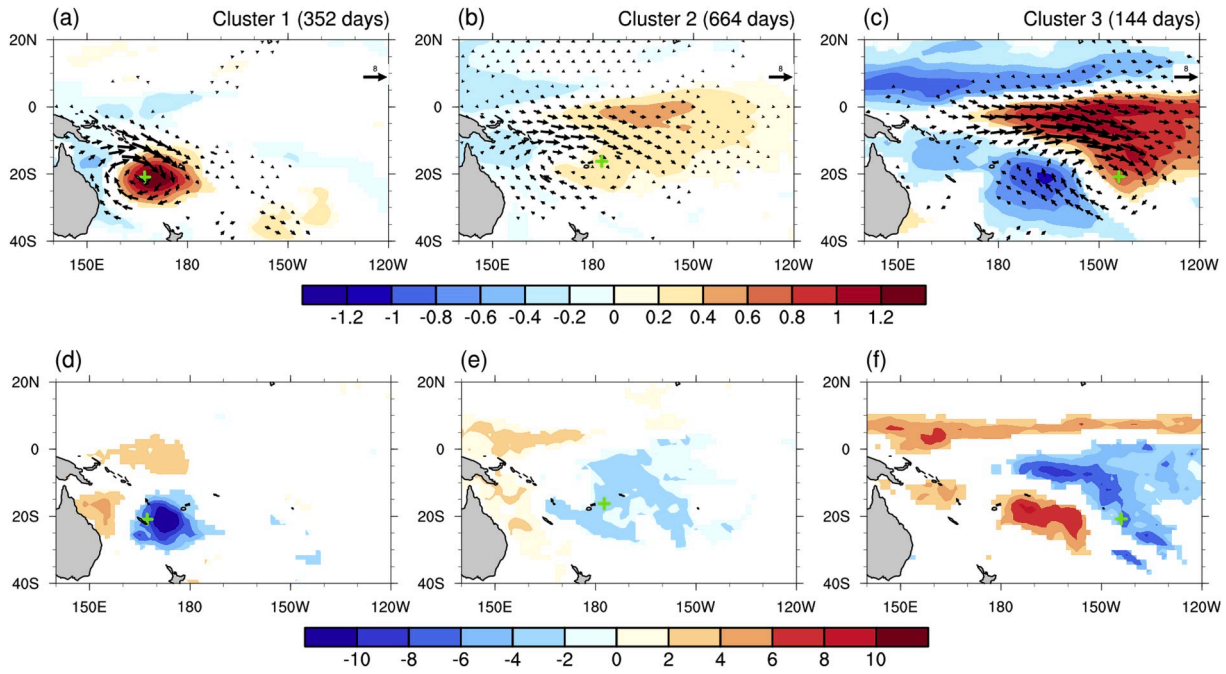

Fig. 9. Anomaly composites of (a–c) vertically integrated specific humidity (shaded, kg kg^{-1}) and 850 hPa wind (vectors, m s^{-1}), (d–f) vertically integrated moisture flux divergence (10^{-5} kg m^{-2} s^{-1}), for all TCDs in cluster 1 (left panel), cluster 2 (middle panel), and cluster 3 (right panel). Only significant values at the 95% confidence level are shown, computed using a bootstrap resampling method by randomizing the time series 1 000 times. The approximate central location relative to the stations in each cluster is represented by a green marker with a plus sign. (For interpretation of the references to colour in this figure legend, the reader is referred to the Web version of this article.)

significant amplification of cyclonic circulation, enhancement of northwesterly flow, and moisture convergence. In particular, to the northeast of the cyclonic center, the transport of moisture by northwesterly winds appears to contribute to the moisture convergence in all three clusters. It is interesting to note that the anomalies of wind, specific humidity, and moisture divergences are weaker in cluster 2 compared to the remaining two clusters. The likely reason for this is the higher number of TCDs (TCD∼664) in cluster 2 and the greater geographic distribution of stations compared to cluster 1 (TCD∼352) and cluster 3 (TCD∼144); as the averaging over space and events will smooth and weaken the atmospheric conditions. Even though the anomalies are weak in the case of cluster 2, they are significant at the 95% confidence level.

As for TCs, we investigate the modulation of moisture convergence by the MJO as a mechanism for extreme rainfall events in all three clusters. We focus on moisture convergence, as it plays a key role in providing favorable conditions for extreme rainfall events while the local evaporation does not directly contribute (Fig. 6d–f). During MJO phases 5, 7, and 8, the atmospheric circulation patterns corresponding to extreme rainfall events in each cluster seems to be enhanced by the circulation change related to the MJO (Fig. 10b,d,f). In all three cases, northwesterly wind anomalies are present that help to strengthen the general northwesterly wind patterns associated with extreme rainfall events. Associated with these wind anomalies there is net moisture convergence and increased vertically integrated specific humidity. In contrast, during the opposite MJO phases, the wind anomalies are from the southeast; hence the wind circulations weaken in phases 1, 3, and 4, and there is net moisture divergence with reduced vertically integrated specific humidity (Fig. 10a,c,e). This suggests that the MJO can increase (decrease) the chance of extreme rainfall events through the related circulation changes that transport moisture from equatorial regions to (decrease) increase moisture at the cluster locations; this helps to strengthen (weaken) the disturbances shown in Fig. 6, thereby promoting (suppressing) extreme rainfall events. This effect depends on the MJO phase and location of the cluster.

In the case of ENSO, we compute similar composites for El-Niño and La-Niña conditions for all available days in November–April over the study period (Fig. 11). Unlike TCs and the MJO, the mechanisms are less obvious. In cluster 1, during La-Niña conditions, a weak but statistically significant northwesterly wind anomaly is apparent to the southwest of the mean SPCZ (Fig. 11b). The positive specific humidity anomalies are consistent with the northwesterly flow. As a result, moisture convergence is also enhanced. This could explain the increased occurrence of extreme rainfall events during La-Niña conditions (Fig. 5a). In contrast, during El-Niño conditions, the southeasterly wind anomalies dominate the region with the relatively dry atmospheric condition and suppress moisture convergence (Fig. 11a); but there is little impact on extreme probability (Fig. 5a).

However, in the case of cluster 2 and cluster 3, the changes in the background state during different phases of ENSO and its implication to extreme rainfall events are less obvious. In particular, changes in the background state of moisture and associated moisture divergence are not systematic. During El-Niño conditions, the atmosphere is slightly dry with moisture divergence in cluster 2, while little or no change in the background state of moisture is observed in cluster 3. Thus, these changes cannot explain the increase in the probability of extreme rainfall events found in cluster 3 during El-Niño events (Fig. 5b). On the other hand, during La-Niña conditions, the general atmospheric condition is dry in cluster 3, but slightly positive to no change in specific humidity anomalies are observed in cluster 2. These changes are consistent with the decrease in the probability of extremes during La-Niña in cluster 3, but cannot explain the decrease in cluster 2 (Fig. 5b and c).

In general, we observe a considerable shift in wind circulation and moisture convergence to the southwest and northeast of the mean SPCZ during La-Niña and El-Niño conditions. Such a shift in background atmospheric conditions provides favorable (less favorable) conditions for extreme rainfall events by supplying more heat and moisture to the atmosphere. These changes, however, do not correspond completely to the observed changes in extreme rainfall events, and further work is

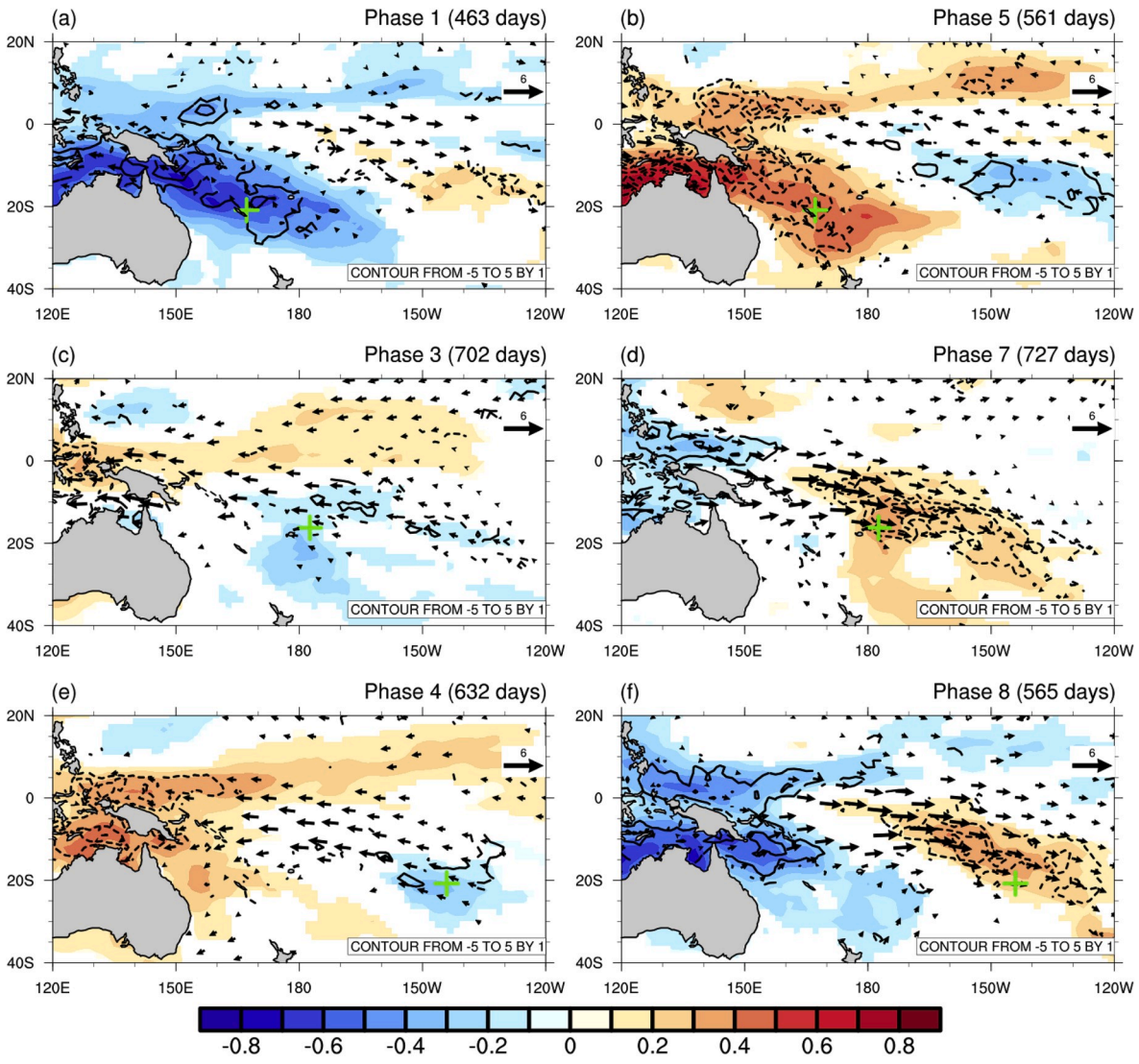

Fig. 10. Anomaly composites of vertically integrated specific humidity (shaded, kg kg^{-1}), vertically integrated moisture flux divergence (contours, 10^{-5} kg m^{-2} s^{-1}), and 850 hPa wind (vectors, m s^{-1}) for selected MJO phases. Only significant values at the 95% confidence level are shown, computed using a bootstrap resampling method by randomizing the time series 1 000 times. The approximate central location relative to the stations in each cluster is represented by a green marker with a plus sign. The dashed (solid) contours represent negative (positive) values. (For interpretation of the references to colour in this figure legend, the reader is referred to the Web version of this article.)

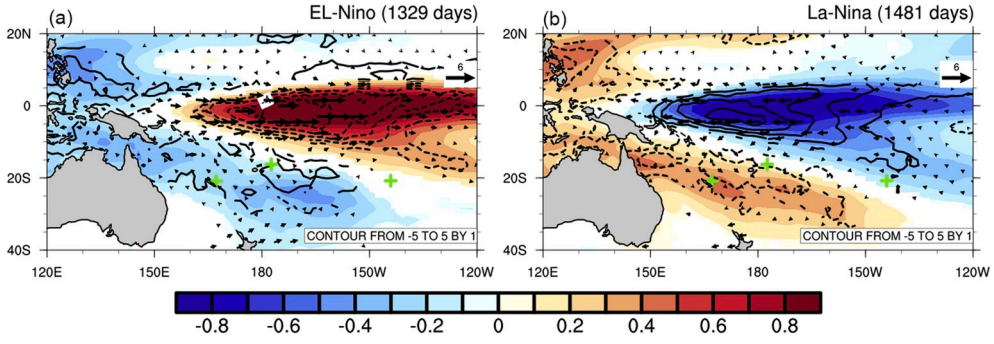

Fig. 11. Anomaly composites of vertically integrated specific humidity (shaded, kg kg^{-1}), vertically integrated moisture flux divergence (contours, 10^{-5} kg m^{-2} s^{-1}), and 850 hPa wind (vectors, m s^{-1}) for ENSO phases. Only significant values at the 95% confidence level are shown, computed using a bootstrap resampling method by randomizing the time series 1 000 times. The approximate central location relative to the stations in each cluster is represented by a green marker with a plus sign. The dashed (solid) contours represent negative (positive) values. (For interpretation of the references to colour in this figure legend, the reader is referred to the Web version of this article.)

required to understand the ENSO impact on extreme rainfall events in this region.

5. Summary and discussion

We investigate the impact of TCs, MJO, ENSO, and extratropical Rossby waves on extreme rainfall events in the South Pacific from 1979 to 2018 based on daily station and reanalysis data sets. From a probabilistic point of view, TCs are the most important factors affecting the occurrence of extreme rainfall events over the South Pacific, followed by the MJO and ENSO. Extratropical Rossby waves do not seem to have significant impact on extreme rainfall events in the South Pacific, however, they can generate necessary disturbances that can develop into extreme rainfall events.

The most significant impact of TCs is observed in cluster 1, where there are, in general, a higher number of TCs (Dowdy et al., 2012). This is also the region with the most intense TCs (Dowdy et al., 2012). Thus, it is not surprising that the impact of TCs is more pronounced in cluster 1. However, the considerably lower impact of TCs on the probability of extremes in cluster 2 needs further explanation. The occurrence of less intense TCs along the SPCZ compared to the region west and east of the SPCZ is one possible reason (Fig. 4, Dowdy et al., 2012). The total number of TCD observed in cluster 2 is significantly higher (TCD∼664) than in cluster 1 (TCD∼352), but the number of TC induced extreme rainfall events in the two clusters are comparable ($TCD_{cluster1}$∼55 and $TCD_{cluster2}$∼57). This suggests that even if there are a substantial number of TCDs, only a few TCs produce extreme rainfall events in cluster 2. Likewise, the relatively bigger impact of TC on the probability of extreme rainfall events in cluster 3 than cluster 2 is also likely because of more intense TCs in the far eastern SPCZ compared to the central SPCZ (Fig. 4, Dowdy et al., 2012).

The most extreme rainfall events in cluster 1 are associated with TCs; while for the other two clusters, it is not clear what synoptic phenomena drive the most extreme rainfall events. Furthermore, our analysis suggests that neither tropical depressions nor extratropical Rossby waves contribute to the most extreme rainfall events in cluster 2 and cluster 3. Therefore, which synotpic scale phenomena are most important for driving extreme rainfall events in these two regions remains an open question that needs further study.

The convective phases of the MJO over the South Pacific are linked to the increased frequency of extreme rainfall events. In particular, MJO phases 1, 5, 6, 7, and 8 are associated with a higher probability of extreme rainfall events in the South Pacific. Matthews and Li (2005) observed a significant impact of the MJO on daily station rainfall over the South Pacific. They identified four different categories of the large-scale rainfall structures over the western Pacific, and three of them correspond to the respective OLR composites for cluster 1, cluster 2, and cluster 3 in our analysis. Similarly, these three large-scale rainfall structures are consistent with the MJO phase composites of OLR anomalies for MJO phases 5, 7, and 8 (Fig. 4h,i,k). Furthermore, Jones et al. (2004) investigated the impact of the MJO on the occurrence of global rainfall extremes by using the pentad GPCP rainfall data. They also identified four leading OLR patterns similar to that of Matthews and Li (2005), and three of them correspond to MJO phases 5, 7, and 8. They further concluded that these large-scale patterns are associated with the higher frequency of extreme rainfall events over the South Pacific (Fig. 6, Jones et al., 2004). Our results are consistent with the findings of these studies.

The impact of ENSO on the occurrence of extreme rainfall events is less clear, particularly for cluster 2 and cluster 3. For cluster 1, the increase (decrease) in the probability of extreme rainfall events during the positive (negative) phase of ENSO is somewhat related to the southwestward (northeastward) shift of SPCZ. Such a displacement of SPCZ tends to shift the warm and moist regime that can support more extreme rainfall events. For cluster 2 and cluster 3, even though the probability estimates show a statistically significant change in probability during ENSO phases, the large-scale patterns of OLR, surface wind, and moisture convergence are not consistent with the changes in probabilities. One possible explanation for this could be the choice of cluster size. It is evident from Figs. 5 and 11 that the stations in cluster 2 and cluster 3 are distributed across different ENSO regimes. For example, for cluster 2, during El-Niño condition, the northernmost stations (north of central location of cluster) show more humid atmosphere and moisture convergence, whereas the opposite patterns are observed for the southernmost stations (south of central location of cluster) (Fig. 11). Similarly, for cluster 3, stations to the northeast (southwest) of the central location show opposite patterns during different ENSO phases. It is difficult to cluster limited number of stations that suits all different phenomena considered with different spatial scales. Therefore, to better understand the impact of ENSO on the extreme rainfall events in the South Pacific, the clustering should be revisited by adding more stations in future work.

TC activity over the South Pacific is linked to the phases of MJO and ENSO and therefore, it is interesting to discuss briefly how the combined influence of MJO and TC or ENSO and TC influence extreme rainfall events in the South Pacific. Klotzbach (2014) investigated the impact of the MJO on worldwide TC activity and found that the thermodynamic conditions for TCs is more (less) favorable in the South Pacific during MJO phases 6–8 (2–5). In our case, we also found considerably higher frequencies of TCs during extreme rainfall events in phases 6–8 compared to phases 2–5. There are 24, 23, and 8 TCs in cluster 1, cluster 2, and cluster 3, respectively that are associated with extreme rainfall events in phase 5–8, whereas only 9, 14, and 2 TCs are observed during phases 2–5. This suggests that the increased (decreased) probability of extreme rainfall events during certain phases of MJO may be partly related to the MJO induced changes in TC activity. In the case of ENSO, the displacement of the SPCZ during ENSO events is also found to modulate TC activity. For example, as the SPCZ migrates to the southwest during La-Niña events, TC activity also increases in this region because the conditions are more favorable for TCs (Revell and Goulter, 1986; Hastings, 1990; Basher and Zheng, 1995; Kuleshov et al., 2008). Therefore, the modulation of probability of extreme rainfall events during different ENSO phases can also be partly related to changes in TC activity. The number of TCDs is relatively high during La-Niña conditions in cluster 1 (n∼15) and during El-Niño conditions in cluster 2 (n∼17) and cluster 3 (n∼8). For the opposite ENSO phase the corresponding numbers are lower (7, 8, and 0 in cluster 1, cluster 2, and cluster 3, respectively). Even though the numbers of TCDs are small and the differences between positive and negative phase are not statistically significant, these results are still consistent with previous findings (Basher and Zheng, 1995; Terry, 2007; Dowdy et al., 2012). While these results for combined effects of different phenomena are inconclusive because of the small sample size, we hope they will motivate future work.

Extreme rainfall events in the South Pacific are linked to cyclonic circulation anomalies associated with low-pressure systems. The cyclonic circulation anomalies are found to enhance the northwesterly flow. Such changes in wind circulation are accompanied by the transport of moisture from the equatorial region and enhanced moisture convergence. The increase in moisture convergence due to the enhancement of the wind circulation is the key mechanism for extreme rainfall events during TCDs and different phases of the MJO. A similar mechanism has been proposed by Ren and Ren (2017) while studying the impact of the MJO on extreme rainfall events in Southern China. In particular, the modulation of circulation and moisture during TCDs and active MJO phases in the South Pacific can lead to more or less suitable conditions for extreme rainfall events.

Apart from MJO, ENSO, and TCs, we also found a link between extratropical Rossby waves and the synoptic conditions associated with extreme rainfall events in all three clusters. The propagation of wave energy two days prior to extreme rainfall events from the subtropical region to the low-pressure center is evident in all three clusters. The

impact of extratropical disturbances on tropical convection is shown by various studies (Lim and Chang, 1981; Webster and Holton, 1982; Weickmann, 1983; Liebmann and Hartmann, 1984; Slingo, 1998; Yoneyama and Parsons, 1999; Knippertz, 2005; Allen et al., 2009). In particular, Hoskins and Yang (2000) suggested that extratropical waves could lead to a perturbation of the equatorial waveguide that further helps to organize convection in the tropical region. However, the frequent occurrence of extratropical wave events does not substantially change the probabilities of extreme rainfall events in the South Pacific.

The understanding of present climate can be useful for understanding future climate change. Thus, we compare our results with the main findings of present and future changes in extreme events from the Intergovernmental Panel on Climate Change (IPCC) report on climate change. The IPCC fifth assessment report concluded with high confidence that the small island countries over the South Pacific are highly vulnerable to climate related extreme events (Field et al., 2012; Stocker et al., 2013). The mean rainfall is projected to increase in the future with more extreme rainfall events for many island nations in the South Pacific. The fifth assessment report has identified TCs as one of the main drivers of climatic extreme events in the South Pacific. We also show that TCs are the most important factor for extreme rainfall events in the South Pacific. Furthermore, it is projected that the average maximum intensities of TCs will be increased in the future climate. Thus, it is likely that the intensities of TC induced extreme rainfall events will also increase in future climate, particularly in cluster 1. Considering these future changes in extreme frequency and intensities of TCs and results from our study, it is interesting to investigate how TCs impact the occurrence and magnitudes of extreme rainfall events in different future climate change scenarios. This might be an interesting topic for future study.

In summary, this study identifies the key factors affecting extreme rainfall events and their mechanisms over the South Pacific. The analysis mostly focuses on the impacts of an individual phenomenon (TCs, ENSO, MJO, extratropical Rossby waves) on extreme rainfall events. Our results should be useful for futures studies on the combined impacts of these phenomena on rainfall extremes in the South Pacific. We hope they will also motivate studies on predictability of extreme rainfall events in this region and on climate change impacts.

Funding

This work is supported by the European Research Council-Synchronisation to Enhance Reliability of Climate Prediction (ERC-STERCP) project (Grant Agreement No-64982).

Declaration of competing interest

The authors declare that they have no competing interests.

CRediT authorship contribution statement

Sunil Kumar Pariyar: Conceptualization, Methodology, Software, Formal analysis, Writing - original draft, Visualization. **Noel Keenlyside:** Supervision, Writing - review & editing, Funding acquisition. **Asgeir Sorteberg:** Methodology, Supervision. **Thomas Spengler:** Supervision, Writing - review & editing. **Bhuwan Chandra Bhatt:** Writing - review & editing. **Fumiaki Ogawa:** Methodology, Writing - review & editing.

Acknowledgments

We thank Michael Reeder and Leonidas Tsopouridis for their valuable inputs during this study. This work is supported by the European Research Council-Synchronisation to Enhance Reliability of Climate Prediction (ERC-STERCP) project (Grant Agreement No-64982).

Appendix A. Supplementary data

Supplementary data to this article can be found online at https://doi.org/10.1016/j.wace.2020.100262.

Abbreviations

SPCZ	South Pacific Convergence Zone
TCs	Tropical Cyclones
MJO	Madden-Julian Oscillation
ENSO	El-Niño and Southern Oscillation
NCDC	National Climate Data Center
OLR	Outgoing Longwave Radiation
NOAA	National Oceanic and Atmospheric Administration
GPCP	Global Precipitation Climatology Project
RMM	Real-time Multivariate MJO
OMI	outgoing longwave radiation-based MJO index
SST	Sea Surface Temperature
IBTrACS	International Best Track Archive for Climate Stewardship
TCD	Tropical Cyclone Day
SLP	Sea Level Pressure
Qdiv	moisture divergence
SD	Standard Deviation
IPCC	Intergovernmental Panel on Climate Change
ERC-STERCP	European Research Council-Synchronisation to Enhance Reliability of Climate Prediction

References

Adler, R.F., Huffman, G.J., Chang, A., Ferraro, R., Xie, P.P., Janowiak, J., et al., 2003. The version-2 global precipitation climatology project (GPCP) monthly precipitation analysis (1979–present). J. Hydrometeorol. 4 (6), 1147–1167.

Allen, G., Vaughan, G., Brunner, D., May, P.T., Heyes, W., Minnis, P., Ayers, J.K., 2009. Modulation of tropical convection by breaking Rossywaves. Q. J. R. Meteorol. Soc. 135, 125–137.

Basher, R.E., Zheng, X., 1995. Tropical cyclones in the southwest Pacific: spatial patterns and relationships to Southern Oscillation and sea surface temperature. J. Clim. 8 (5), 1249–1260.

Bettencourt, S., Croad, R., Freeman, P., Hay, J., Jones, R., King, P., et al., 2006. Not if but when: Adapting to Natural Hazards in the Pacific Islands Region. The World Bank.

Borlace, S., Santoso, A., Cai, W., Collins, M., 2014. Extreme swings of the south pacific convergence zone and the different types of el Niño events. Geophys. Res. Lett. 41 (13), 4695–4703.

Brown, J.R., Power, S.B., Delage, F.P., Colman, R.A., Moise, A.F., Murphy, B.F., 2011. Evaluation of the South Pacific Convergence Zone in IPCC AR4 climate model simulations of the twentieth century. J. Clim. 24 (6), 1565–1582.

Callaghan, J., Power, S.B., 2011. Variability and decline in the number of severe tropical cyclones making land-fall over eastern Australia since the late nineteenth century. Clim. Dynam. 37 (3–4), 647–662.

Camargo, S.J., Wheeler, M.C., Sobel, A.H., 2009. Diagnosis of the MJO modulation of tropical cyclogenesis using an empirical index. J. Atmos. Sci. 66 (10), 3061–3074.

Chand, S.S., Dowdy, A., Bell, S., Tory, K., 2020. A review of South Pacific tropical cyclones: impacts of natural climate variability and climate change. In: Climate Change and Impacts in the Pacific. Springer, Cham, pp. 251–273.

Chen, F., Fu, Y., 2015. Contribution of tropical cyclone rainfall at categories to total precipitation over the Western North Pacific from 1998 to 2007. Sci. China Earth Sci. 58 (11).

Chen, Y., Ebert, E.E., Walsh, K.J., Davidson, N.E., 2013. Evaluation of TMPA 3B42 daily precipitation estimates of tropical cyclone rainfall over Australia. J. Geophys. Res.: Atmosphere 118 (21), 11–966.

Dare, R.A., Davidson, N.E., McBride, J.L., 2012. Tropical cyclone contribution to rainfall over Australia. Mon. Weather Rev. 140 (11), 3606–3619.

Dee, D.P., Uppala, S.M., Simmons, A.J., Berrisford, P., Poli, P., Kobayashi, S., et al., 2011. The ERA-Interim reanalysis: configuration and performance of the data assimilation system. Q. J. R. Meteorol. Soc. 137 (656), 553–597.

Diamond, H.J., Lorrey, A.M., Knapp, K.R., Levinson, D.H., 2012. Development of an enhanced tropical cyclone tracks database for the southwest Pacific from 1840 to 2010. Int. J. Climatol. 32 (14), 2240–2250.

Dowdy, A.J., Qi, L., Jones, D., Ramsay, H., Fawcett, R., Kuleshov, Y., 2012. Tropical cyclone climatology of the south pacific ocean and its relationship to el niño–southern oscillation. J. Clim. 25 (18), 6108–6122.

Durre, I., Menne, M.J., Gleason, B.E., Houston, T.G., Vose, R.S., 2010. Comprehensive automated quality assurance of daily surface observations. Journal of Applied Meteorology and Climatology 49 (8), 1615–1633.

Field, C.B., Barros, V., Stocker, T.F., Dahe, Q. (Eds.), 2012. Managing the Risks of Extreme Events and Disasters to Advance Climate Change Adaptation: Special Report of the Intergovernmental Panel on Climate Change. Cambridge University Press.

Folland, C.K., Renwick, J.A., Salinger, M.J., Mullan, A.B., 2002. Relative influences of the interdecadal Pacific oscillation and ENSO on the South Pacific convergence zone. Geophys. Res. Lett. 29 (13), 21-1.
Ghayekhloo, M., Ghofrani, M., Menhaj, M.B., Azimi, R., 2015. A novel clustering approach for short-term solar radiation forecasting. Sol. Energy 122, 1371–1383.
Griffiths, G.M., Salinger, M.J., Leleu, I., 2003. Trends in extreme daily rainfall across the south pacific and relationship to the south pacific convergence zone. *Int. J. Climatol.*: A Journal of the Royal Meteorological Society 23 (8), 847–869.
Hastings, P.A., 1990. Southern Oscillation influences on tropical cyclone activity in the Australian/southwest Pacific region. Int. J. Climatol. 10 (3), 291–298.
He, J., Deser, C., Soden, B.J., 2017. Atmospheric and oceanic origins of tropical precipitation variability. J. Clim. 30 (9), 3197–3217.
Hoarau, K., Chalonge, L., Pirard, F., Peyrusaubes, D., 2018. Extreme tropical cyclone activities in the southern Pacific Ocean. Int. J. Climatol. 38 (3), 1409–1420.
Hoskins, B.J., Yang, G.Y., 2000. The equatorial response to higher-latitude forcing. J. Atmos. Sci. 57 (9), 1197–1213.
Jenkins, A.P., Jupiter, S., 2015. Natural disasters, health and wetlands: a Pacific small island developing state perspective. In: Wetlands and Human Health. Springer, Dordrecht, pp. 169–191.
Jiang, H., Zipser, E.J., 2010. Contribution of tropical cyclones to the global precipitation from eight seasons of TRMM data: regional, seasonal, and interannual variations. J. Clim. 23 (6), 1526–1543.
Jones, C., Waliser, D.E., Lau, K.M., Stern, W., 2004. Global occurrences of extreme precipitation and the Madden–Julian oscillation: observations and predictability. J. Clim. 17 (23), 4575–4589.
Jovanovic, B., Braganza, K., Collins, D., Jones, D., 2012. Climate variations and change evident in high-quality climate data for Australia's Antarctic and remote island weather stations. Aust. Meteorol. Oceanogr. J 62, 247–261.
Kaufman, L., Rousseeuw, P.J., 2009. Finding Groups in Data: an Introduction to Cluster Analysis, vol. 344. John Wiley & Sons.
Ketchen, D.J., Shook, C.L., 1996. The application of cluster analysis in strategic management research: an analysis and critique. Strat. Manag. J. 17 (6), 441–458.
Khouakhi, A., Villarini, G., Vecchi, G.A., 2017. Contribution of tropical cyclones to rainfall at the global scale. J. Clim. 30 (1), 359–372.
Kidson, J.W., Renwick, J.A., 2002. The southern hemisphere evolution of ENSO during 1981–99. J. Clim. 15 (8), 847–863.
Kidwell, A., Lee, T., Jo, Y.H., Yan, X.H., 2016. Characterization of the variability of the South Pacific convergence zone using satellite and reanalysis wind products. J. Clim. 29 (5), 1717–1732.
Kiladis, G.N., Dias, J., Straub, K.H., Wheeler, M.C., Tulich, S.N., Kikuchi, K., et al., 2014. A comparison of OLR and circulation-based indices for tracking the MJO. Mon. Weather Rev. 142 (5), 1697–1715.
Kiladis, G.N., Weickmann, K.M., 1997. Horizontal structure and seasonality of large-scale circulations associated with submonthly tropical convection. Mon. Weather Rev. 125 (9), 1997–2013.
Klotzbach, P.J., 2014. The Madden–Julian oscillation's impacts on worldwide tropical cyclone activity. J. Clim. 27 (6), 2317–2330.
Knapp, K.R., Kruk, M.C., Levinson, D.H., Diamond, H.J., Neumann, C.J., 2010. The international best track archive for climate stewardship (IBTrACS) unifying tropical cyclone data. Bull. Am. Meteorol. Soc. 91 (3), 363–376.
Knippertz, P., 2005. Tropical–extratropical interactions associated with an Atlantic tropical plume and subtropical jet streak. Mon. Weather Rev. 133 (9), 2759–2776.
Kuleshov, Y., McGree, S., Jones, D., Charles, A., Cottrill, A., Prakash, B., et al., 2014. Extreme weather and climate events and their impacts on island countries in the Western Pacific: cyclones, floods and droughts. Atmos. Clim. Sci. 4 (5), 803.
Kuleshov, Y., Qi, L., Fawcett, R., Jones, D., 2008. On tropical cyclone activity in the Southern Hemisphere: trends and the ENSO connection. Geophys. Res. Lett. 35 (14).
Kumar, R., Stephens, M., Weir, T., 2014. Rainfall trends in Fiji. Int. J. Climatol. 34 (5), 1501–1510.
Larson, J., Zhou, Y., Higgins, R.W., 2005. Characteristics of landfalling tropical cyclones in the United States and Mexico: climatology and interannual variability. J. Clim. 18 (8), 1247–1262.
Lee, M.H., Ho, C.H., Kim, J.H., 2010. Influence of tropical cyclone landfalls on spatiotemporal variations in typhoon season rainfall over South China. Adv. Atmos. Sci. 27 (2), 443–454.
Liebmann, B., Hartmann, D.L., 1984. An observational study of tropical–midlatitude interaction on intraseasonal time scales during winter. J. Atmos. Sci. 41 (23), 3333–3350.
Liebmann, B., Smith, C.A., 1996. Description of a complete (interpolated) outgoing longwave radiation dataset. Bull. Am. Meteorol. Soc. 77 (6), 1275–1277.
Lim, H., Chang, C.P., 1981. A theory for midlatitude forcing of tropical motions during winter monsoons. J. Atmos. Sci. 38 (11), 2377–2392.
Madden, R.A., Julian, P.R., 1994. Observations of the 40–50-day tropical oscillation—a review. Mon. Weather Rev. 122 (5), 814–837.
Manton, M.J., Della-Marta, P.M., Haylock, M.R., Hennessy, K.J., Nicholls, N., Chambers, L.E., et al., 2001. Trends in extreme daily rainfall and temperature in southeast asia and the south pacific: 1961–1998. Int. J. Climatol. 21 (3), 269–284.
Matthews, A.J., 2012. A multiscale framework for the origin and variability of the South Pacific Convergence Zone. Q. J. R. Meteorol. Soc. 138 (666), 1165–1178.
Matthews, A.J., Li, H.Y.Y., 2005. Modulation of station rainfall over the western Pacific by the Madden-Julian oscillation. Geophys. Res. Lett. 32 (14).
Matthews, A.J., Hoskins, B.J., Slingo, J.M., Blackburn, M., 1996. Development of convection along the SPCZ within a Madden-Julian oscillation. Q. J. R. Meteorol. Soc. 122 (531), 669–688.
McCarthy, J.J., Canziani, O.F., Leary, N.A., Dokken, D.J., White, K.S., 2001. *Climate Change* 2001.
McGree, S., Herold, N., Alexander, L., Schreider, S., Kuleshov, Y., Ene, E., et al., 2019. Recent changes in mean and extreme temperature and precipitation in the Western Pacific Islands. J. Clim. 32 (16), 4919–4941.
McGree, S., Whan, K., Jones, D., Alexander, L.V., Imielska, A., Diamond, H., et al., 2014. An updated assessment of trends and variability in total and extreme rainfall in the western Pacific. Int. J. Climatol. 34 (8), 2775–2791.
Muñoz, Á.G., Goddard, L., Robertson, A.W., Kushnir, Y., Baethgen, W., 2015. Cross–time scale interactions and rainfall extreme events in southeastern South America for the austral summer. Part I: potential predictors. J. Clim. 28 (19), 7894–7913.
Ng, B., Walsh, K., Lavender, S., 2015. The contribution of tropical cyclones to rainfall in northwest Australia. Int. J. Climatol. 35 (10), 2689–2697.
Niznik, M.J., Lintner, B.R., Matthews, A.J., Widlansky, M.J., 2015. The role of tropical-extratropical interaction and synoptic variability inmaintaining the South Pacific Convergence Zone in CMIP5 models. J. Clim. 28, 3353–3374.
Nogueira, R.C., Keim, B.D., 2011. Contributions of Atlantic tropical cyclones to monthly and seasonal rainfall in the eastern United States 1960–2007. Theor. Appl. Climatol. 103 (1–2), 213–227.
Nurse, L.A., McLean, R.F., Agard, J., Briguglio, L.P., Duvat-Magnan, V., Pelesikoti, N., Tompkins, E., Webb, A., 2014. Small islands. In: Barros, V.R., Field, C.B., Dokken, D. J., Mastrandrea, M.D., Mach, K.J., Bilir, T.E., Chatterjee, M., Ebi, K.L., Estrada, Y.O., Genova, R.C., Girma, B., Kissel, E.S., Levy, A.N., MacCracken, S., Mastrandrea, P.R., White, L.L. (Eds.), Climate Change 2014: Impacts, Adaptation, and Vulnerability. Part B: Regional Aspects.Contribution of Working Group II to the Fifth Assessment Report of the Intergovernmental Panel on ClimateChange. Cambridge University Press, Cambridge, United Kingdom and New York, NY, USA, pp. 1613–1654.
O'Gorman, P.A., Schneider, T., 2009. The physical basis for increases in precipitation extremes in simulations of 21st-century climate change. Proc. Natl. Acad. Sci. Unit. States Am. 106 (35), 14773–14777.
Pariyar, S.K., Keenlyside, N., Chandra Bhatt, B., Omrani, N.E., 2019. The dominant patterns of intraseasonal rainfall variability in may–october and november–april over the tropical western pacific. Mon. Weather Rev. 147 (8), 2941–2960.
Philander, S.G., 1990. El Niño, La Niña, and the Southern Oscillation (No. 04). GC296. 8. E4, P4.).
Prat, O.P., Nelson, B.R., 2013. Mapping the world's tropical cyclone rainfall contribution over land using the TRMM Multi-satellite Precipitation Analysis. Water Resour. Res. 49 (11), 7236–7254.
Rayner, N.A.A., Parker, D.E., Horton, E.B., Folland, C.K., Alexander, L.V., Rowell, D.P., et al., 2003. Global analyses of sea surface temperature, sea ice, and night marine air temperature since the late nineteenth century. J. Geophys. Res.: Atmosphere 108 (D14).
Ren, H.L., Ren, P., 2017. Impact of madden–julian oscillation upon winter extreme rainfall in southern China: observations and predictability in CFSv2. Atmosphere 8 (10), 192.
Revell, C.G., Goulter, S.W., 1986. South Pacific tropical cyclones and the southern oscillation. Mon. Weather Rev. 114 (6), 1138–1145.
Robertson, A.W., Ghil, M., 1999. Large-scale weather regimes and local climate over the western United States. J. Clim. 12 (6), 1796–1813.
Rodgers, E.B., Adler, R.F., Pierce, H.F., 2001. Contribution of tropical cyclones to the North Atlantic climatological rainfall as observed from satellites. J. Appl. Meteorol. 40 (11), 1785–1800.
Rousseeuw, P.J., 1987. Silhouettes: a graphical aid to the interpretation and validation of cluster analysis. J. Comput. Appl. Math. 20, 53–65.
Salinger, M.J., Lefale, P., 2005. The occurrence and predictability of extreme events over the Southwest Pacific with particular reference to ENSO. Natural Disasters and Extreme Events in Agriculture. Springer, Berlin, Heidelberg, pp. 39–49.
Salinger, M.J., McGree, S., Beucher, F., Power, S.B., Delage, F., 2014. A new index for variations in the position of the South Pacific convergence zone 1910/11–2011/2012. Clim. Dynam. 43 (3–4), 881–892.
Salinger, M.J., Renwick, J.A., Mullan, A.B., 2001. Interdecadal Pacific oscillation and south Pacific climate. Int. J. Climatol. 21 (14), 1705–1721.
Slingo, J.M., 1998. Extratropical forcing of tropical convection in a northern winter simulation with the UGAMP GCM. Q. J. R. Meteorol. Soc. 124 (545), 27–51.
Stocker, T.F., Qin, D., Plattner, G.K., Tignor, M., Allen, S.K., Boschung, J., et al., 2013. Climate Change 2013: the Physical Science Basis. *Contribution Of Working Group I to the Fifth Assessment Report of the Intergovernmental Panel on Climate Change*, p. 1535.
Takaya, K., Nakamura, H., 1997. A formulation of a wave-activity flux for stationary Rossby waves on a zonally varying basic flow. Geophys. Res. Lett. 24 (23), 2985–2988.
Takaya, K., Nakamura, H., 2001. A formulation of a phase-independent wave-activity flux for stationary and migratory quasigeostrophic eddies on a zonally varying basic flow. J. Atmos. Sci. 58 (6), 608–627.
Terry, J.P., 2007. Tropical Cyclones: Climatology and Impacts in the South Pacific. Springer Science & Business Media.
Tibshirani, R., Walther, G., Hastie, T., 2001. Estimating the number of clusters in a data set via the gap statistic. J. Roy. Stat. Soc. B 63 (2), 411–423.
Trenberth, K.E., 1976. Spatial and temporal variations of the southern oscillation. Q. J. R. Meteorol. Soc. 102 (433), 639–653.
Trenberth, K.E., 1997. The definition of el Niño. Bull. Am. Meteorol. Soc. 78 (12), 2771–2778.
Van Der Wiel, K., Matthews, A.J., Joshi, M.M., Stevens, D.P., 2016a. The influence of diabatic heating in the South Pacific Convergence Zone on Rossby wave propagation and the mean flow. Q. J. R. Meteorol. Soc. 142 (695), 901–910.
Van Der Wiel, K., Matthews, A.J., Joshi, M.M., Stevens, D.P., 2016b. Why the South Pacific convergence zone is diagonal. Clim. Dynam. 46 (5–6), 1683–1698.

Van Der Wiel, K., Matthews, A.J., Stevens, D.P., Joshi, M.M., 2015. A dynamical framework for the origin of the diagonal South Pacific and South Atlantic convergence zones. Q. J. R. Meteorol. Soc. 141 (691), 1997–2010.
Villarini, G., Lavers, D.A., Scoccimarro, E., Zhao, M., Wehner, M.F., Vecchi, G.A., et al., 2014. Sensitivity of tropical cyclone rainfall to idealized global-scale forcings. J. Clim. 27 (12), 4622–4641.
Vincent, D.G., 1994. The South Pacific convergence zone (SPCZ): a review. Mon. Weather Rev. 122 (9), 1949–1970.
Vincent, E.M., Lengaigne, M., Menkes, C.E., Jourdain, N.C., Marchesiello, P., Madec, G., 2011. Interannual variability of the South Pacific Convergence Zone and implications for tropical cyclone genesis. Clim. Dynam. 36 (9–10), 1881–1896.
Vincent, L.A., Wang, X.L., Milewska, E.J., Wan, H., Yang, F., Swail, V., 2012. A second generation of homogenized Canadian monthly surface air temperature for climate trend analysis. J. Geophys. Res.: Atmosphere 117 (D18).
Wallace, J.M., Gutzler, D.S., 1981. Teleconnections in the geopotential height field during the Northern Hemisphere winter. Mon. Weather Rev. 109 (4), 784–812.
Walsh, K.J., McBride, J.L., Klotzbach, P.J., Balachandran, S., Camargo, S.J., Holland, G., et al., 2016. Tropical cyclones and climate change. Wiley Interdisciplinary Reviews: Climate Change 7 (1), 65–89.
Wang, X.L., 2008a. Penalized maximal F test for detecting undocumented mean shift without trend change. J. Atmos. Ocean. Technol. 25 (3), 368–384.
Wang, X.L., 2008b. Accounting for autocorrelation in detecting mean shifts in climate data series using the penalized maximal t or F test. Journal of applied meteorology and climatology 47 (9), 2423–2444.
Wang, X. L. and Y. Feng. (published online July 2013). RHtestsV4 user manual. Climate research division, atmospheric science and Technology directorate, science and Technology Branch, Environment Canada. 28 pp. (Available online at http://etccdi.pacificclimate.org/software.shtml).
Wang, X.L., Chen, H., Wu, Y., Feng, Y., Pu, Q., 2010. New techniques for the detection and adjustment of shifts in daily precipitation data series. Journal of Applied Meteorology and Climatology 49 (12), 2416–2436.
Wang, X.L., Wen, Q.H., Wu, Y., 2007. Penalized maximal t test for detecting undocumented mean change in climate data series. Journal of Applied Meteorology and Climatology 46 (6), 916–931.
Webster, P.J., Holton, J.R., 1982. Cross-equatorial response to middle-latitude forcing in a zonally varying basic state. J. Atmos. Sci. 39 (4), 722–733.
Weickmann, K.M., 1983. Intraseasonal circulation and outgoing longwave radiation modes during Northern Hemisphere winter. Mon. Weather Rev. 111 (9), 1838–1858.
Wheeler, M.C., Hendon, H.H., 2004. An all-season real-time multivariate MJO index: development of an index for monitoring and prediction. Mon. Weather Rev. 132 (8), 1917–1932.
Widlansky, M.J., Webster, P.J., Hoyos, C.D., 2011. On the location and orientation of the south pacific convergence zone. Clim. Dynam. 36 (3–4), 561–578.
Yoneyama, K., Parsons, D.B., 1999. A proposed mechanism for the intrusion of dry air into the tropical western Pacific region. J. Atmos. Sci. 56 (11), 1524–1546.
Zhang, C., 2005. Madden-julian oscillation. Rev. Geophys. 43 (2).
Zhang, C., 2013. Madden–Julian oscillation: bridging weather and climate. Bull. Am. Meteorol. Soc. 94 (12), 1849–1870.
Zhang, H., Clement, A., Di Nezio, P., 2014. The South Pacific meridional mode: a mechanism for ENSO-like variability. J. Clim. 27 (2), 769–783.
Zhang, Q., Wu, L., Liu, Q., 2009. Tropical cyclone damages in China 1983–2006. Bull. Am. Meteorol. Soc. 90 (4), 489–496.
Zhao, C., Li, T., Zhou, T., 2013. Precursor signals and processes associated with MJO initiation over the tropical Indian Ocean. J. Clim. 26 (1), 291–307.